

Urban Air Taxi Wing Design

EGR299

William Tohlen

Reviewed by C.S. Lynch, Ph. D.

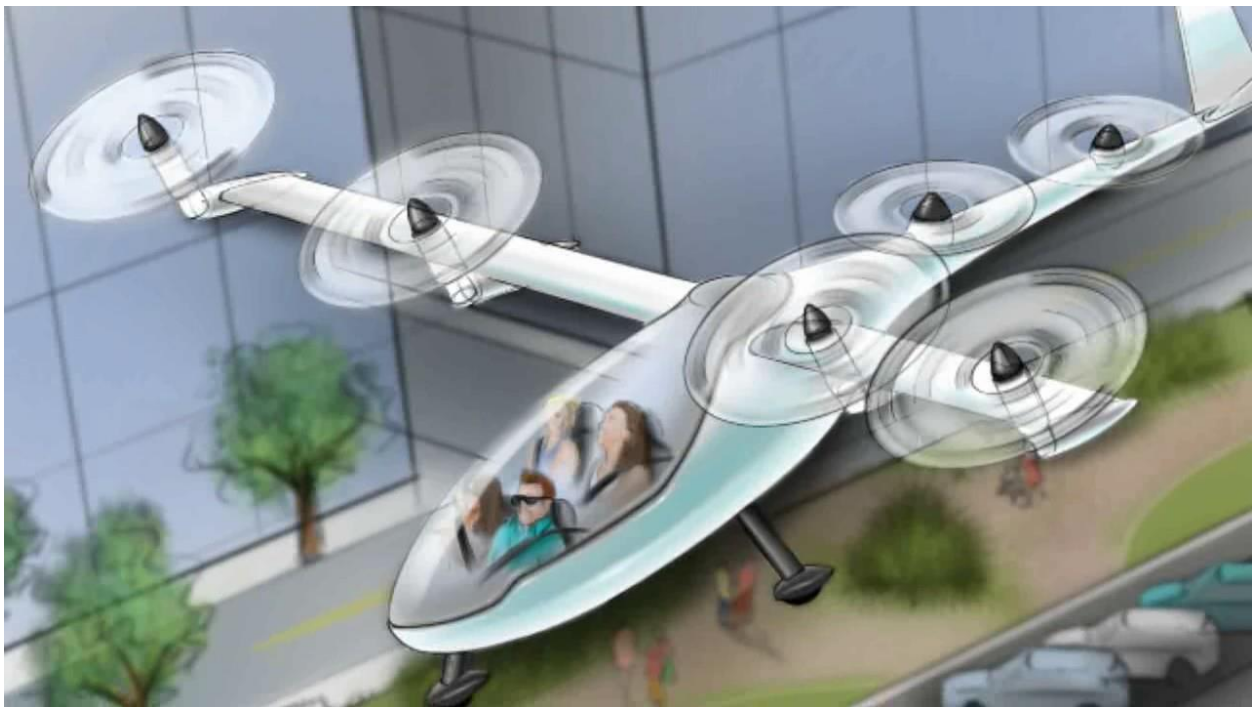


Table of Contents

1	Objective of Wing Design Project	4
2	Requirements.....	6
3	Propulsion	6
4	Wing Design	8
5	Airfoil Selection	8
6	Wing Redesign	14
7	Load Cases.....	18
	7.1 Hover/Takeoff	18
	7.2 Hard Landing	20
	7.3 Transitional	20
	7.4 Steady Flight and Rapid Pull Up from a Dive	21
	7.5 Gust Loads.....	23
8	Strut Design.....	27
9	Analysis	28
10	Results.....	34
11	Margin Summary.....	47
12	Finite Element Validation.....	49
13	Composite Weight Savings.....	52
14	Closing Statement	53
15	Works Cited.....	54

List of Figures

Figure 1 – NASA GL-10 Greased Lightning Tilt-Wing	5
Figure 2 – Bell-Boeing V-22 Osprey Tilt-Rotor	5
Figure 3 – Wing Structure (Top Down)	8
Figure 4 – Cessna 402	9
Figure 5 – NACA 23018 Airfoil.....	10
Figure 6 – XFOIL output for NACA 23018, AoA = 6 deg	11
Figure 7 – NACA 23018 Lift Slope at Sea Level	12
Figure 8 – NACA 23018 Lift Slope at 8,000 ft.....	13
Figure 9 – Cessna 172 Skyhawk Silhouette	15
Figure 10 – Wing Layout [Redesign]	15
Figure 11 – NACA 23018 Lift Slope at Sea Level [Redesign]	16
Figure 12 – NACA 23018 Lift Slope at Altitude [Redesign]	17
Figure 13 – Hover/Take-Off Load Case Free Body Diagram.....	18
Figure 14 – Free Body Diagram for Takeoff/Landing – Front View	19
Figure 15 – Free Body Diagram for Takeoff/Landing – Wing Only	20
Figure 16 – 45° Transition to Forward Flight Load Case	21
Figure 17 – Steady Level Flight.....	22
Figure 18 – Rapid Pull Up from Dive	22
Figure 19 – V-n Diagram for Sea Level	24
Figure 20 – V-n Diagram for 8,000 feet.....	24
Figure 21 – Cantilevered Beam with Simple Support	27
Figure 22 – LC3 45deg Flight Y-Load Distribution	29
Figure 23 – LC3 45deg Flight X-Load Distribution	30
Figure 24 – Coordinate transformation	31
Figure 25 – LC3 45deg Flight	32
Figure 26 – LC3 45deg Flight Shear Diagram	33
Figure 27 – LC3 45deg Flight Moment Diagram	34
Figure 28 – Wing Box Stringer Placement.....	35
Figure 29 – LC3 45deg Flight, Tip deflection	37
Figure 30 – LC3 45deg Flight Normal Stress at Root.....	38

Figure 31 - LC3 45deg Flight Normal Stress at Strut	39
Figure 32 – LC3 45deg Flight Normal Stress	40
Figure 33 – LC2 Takeoff/Hover Rib Distribution	41
Figure 34 – Skin Panel versus Boom Panel.....	42
Figure 35 – LC3 45deg Flight Shear Stress at Root.....	43
Figure 36 - LC3 45deg Flight Shear Stress before Strut.....	44
Figure 37 - LC3 45deg Flight Shear Stress after Strut.....	44
Figure 38 - LC3 45deg Flight Shear Stress at Tip	45
Figure 39 - LC3 45deg Flight Shear Stress over Span	46
Figure 40 – Von Mises Stress LC3 45deg flight	47
Figure 40 – LC 2 Takeoff Von Mises Stress Patran	50
Figure 41 – LC2 Takeoff Von Mises Stress Matlab Plot with Visual Aspect Ratio 1:1:1	51
Figure 42 – LC2 Takeoff Von Mises Stress Matlab Plot.....	51
Figure 43 – LC2 Takeoff/Hover Composite Wing Box Von Mises Stress.....	53

List of Tables

Table 1 – Reynold’s Number	12
Table 2 – 2D and 3D Airfoil Data	13
Table 3 – Reynolds Number [Redesign]	16
Table 4 – 2D and 3D Airfoil Data [Redesign]	17
Table 5 – Critical Load Cases	26
Table 6 – Structure Sizing and Material Properties	35
Table 7 – Margins.....	48
Table 8 – Matlab and FEM Comparison	49

1 Objective of Wing Design Project

In October of 2016, Uber published a white paper that ignited the imagination of the civil aviation industry. The paper described being able to hail a taxi in a city that would be able rise above the traffic and skyscrapers to quickly fly to your destination across town. Uber argued that in the next decade an urban air taxi would become economically feasible and potentially revolutionize commuting in congested environments. Aerospace companies such as Airbus, Boeing, and Bell Helicopter started building prototypes and mock ups to gain early foot holds in a market that could demand up to 5000 vehicles per year (01). For comparison, the bestselling helicopter today is the Robinson R44 averaging 350 (with a maximum of 750) vehicles produced a year (02).

The vehicle in question would need to take off and land vertically, achieve a cruise speed of 150 MPH, and have a range of 50 miles. Modern helicopters meet these demands but Uber argues that they are the incorrect choice for their flying ride sharing service. A helicopter has a large rotor blade that spins at relatively low speeds, making it fuel efficient and powerful in hover at the cost of loud noise and inefficient in forward flight. An air taxi however, needs to be quiet, efficient at cruise, and will not require lifting heavy loads. They propose the solution is a vehicle with several small and fast rotors that can tilt forward in flight. Current examples of this technology would be a tilt-rotor such as the Bell-Boeing V-22 Osprey or a tilt-wing such as the NASA GL-10 Greased Lightning.



Figure 1 – NASA GL-10 Greased Lightning Tilt-Wing



Figure 2 – Bell-Boeing V-22 Osprey Tilt-Rotor

The objective of this report is to optimize the wing structure of an urban air taxi. A tilt rotor design will be proposed with consideration for conventional and electric propulsion. A tilt wing was ruled out as a design due to several drawbacks. The wing would need to pivot at the root next to the fuselage, which is the location of maximum moment on the wing. This would lead to the design of a large rotating shaft through

the wing to allow rotation but resist bending. A tilt rotor by comparison needs to only rotate at the wing tip, where moment is smallest, leading to weight and complexity savings. Additionally, the tilt wing in forward flight would be stalled until a low angle of tilt, like conventional airplanes. A tilt rotor has the benefit of being able to set its rotors at a large range of angles in forward flight while keeping the wing away from stall. This allows the wing to contribute to lift increasing maneuverability while lowering thrust required. To begin, the design parameters would be chosen from the requirements given in the Uber White paper.

2 Requirements

The white paper conjects that the future urban air taxi will be certified under the FAA's powered lift category for VTOL (Vertical Take-Off and Landing) aircraft. However, that category of the Code of Federal Regulations (CFR) does not exist yet. This paper will utilize Part 23 for normal category fixed wing aircraft and Part 27 for normal category rotorcraft (03). The wing will be designed for a 150 mph cruise speed and a 200 mph dive speed. The ceiling will be 8,000 ft. The airfoil shape and wing properties will be discussed in Section 5. It is assumed the aircraft carries enough fuel for a 200 mile flight without reserves. This is assumed to be equivalent to a 50 mile flight with reserves and enough power for an aborted take-off and landing (01). How to account for the weight of the fuel is discussed in the next section.

3 Propulsion

The limiting factor to on-demand air travel as Uber envisions it, is propulsion. Conventional aerospace propulsion involves a turboshaft engine with jet fuel that drives the rotors through a series of gearboxes. The number of critical parts makes this system expensive to design, build, and maintain. Operational costs of helicopters are 200 dollars per hour at the very low end for an R44 and can go up to 10,000 dollars per hour to a machine as complicated as a V-22 (04) (05). A car costs 54 cents a mile to operate (06). For Uber to offer an on-demand air service that is price competitive to a taxi service, operational costs need to come way down. Uber's solution is an electric vehicle. The price to build and maintain engines and gearboxes and the fuel that runs them goes away if you choose a separate dedicated electric motor to directly drive each rotor. The problem is modern batteries are heavy and cannot carry enough charge to sustain flight. The Robinson R44 Cadet carries 177 lbs of fuel in its main tank alone. At max continuous power of 185 hp, the R44 burns through 20 gallons per hour. Assuming aviation fuel weighs 6 pounds per

gallon, the main tank would run dry in less than an hour and a half (04). If the R44 ran off the battery that powers a Tesla, the Panasonic NCR18650B that has an energy density of 243 Wh/kg, the helicopter would need to carry over 18,000 pounds of the batteries to operate for the same amount of time at the same power level (07). Even if the electric motor ran at 2 or 3 times higher efficiency so that the power required was reduced, the weight of the batteries would dwarf the 2,200 lb aircraft. But batteries are getting better and Uber argues that in the next five years batteries will have enough energy density to power the VTOLs of the future. They point to the Department of Energy Battery 500 program that is spending 50 million dollars in research to develop a 500 Wh/kg battery by 2020. Even then, these batteries will have 20 to 30 times less energy density than jet fuel limiting the range of an eVTOL aircraft. A short-term solution could be a hybrid aircraft that utilizes energy dense fuel to drive a motor that recharges the batteries of the electric motor. The gearboxes and drive shafts are removed lowering complexity, and the high weight penalty of storing energy in batteries is avoided. There are many possible solutions but this report will only consider the conventional propulsion of today's world as well as the all-electric propulsion systems of our future.

Assuming the R44 dedicates 30% of its 1440 lb empty weight to the engine and drives components, the propulsion system weighs 432 lbs. With the 177 lbs of fuel needed to operate for 90 mins at max continuous power, the possible weight savings from removing conventional propulsion maxes out at 610 lbs. Next, equation 1 shows the rotor system of the R44 needs 100 hp to hover at max gross weight.

$$P = \sqrt{\frac{T^3}{2\rho A}}$$

$$\sqrt{2200lb^3/(2 * .002sl/ft^3 * 855ft^2)} \tag{1}$$

$$= 55,000 ft \frac{lb}{s} = 100 hp$$

This means the efficiency of the drive train and rotors is around 55%. Assuming an electric motor could achieve near 100% efficiency (after all, this is the future) and use batteries with 500 Wh/kg energy densities, the aircraft would need to carry around 490 lbs of batteries. Once you add the weight of the electric motors to the weight of batteries (such as a Siemens electric motor that is 110 lbs capable of producing over 300 hp (08)), you would get a number in the ball park of the 610 lb propulsion/fuel system of today's R44. Therefore, the analysis presented here assumed there was no weight difference between an aircraft with conventional propulsion versus electric propulsion. This analysis also ignores the benefit

of conventional propulsion burning fuel, thus reducing the weight of the aircraft and the power required throughout a flight.

4 Wing Design

The wing structure will consist of a forward and rear spar as shown in Figure 3. The skin panels will be supported by ribs to resist skin buckling and stringers to support bending loads.

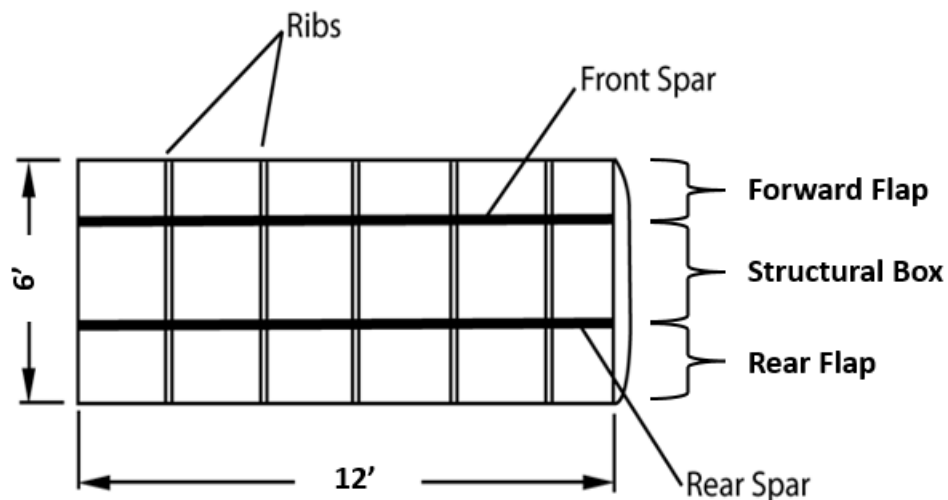


Figure 3 – Wing Structure (Top Down)

The forward and rear boxes of the wing are non-structural flaps than can be turned down during take-off and hover to reduce downwash impingement on the wing. This will reduce the thrust of the rotor that is wasted by pushing down on the wing. For simplicity, the wing will have the same airfoil shape and size down the length of the wing. It will have no taper or twist, and will not be swept.

To reduce the moment at the wing root, a short wing length is desirable, around 12 feet. This is a tradeoff that will necessitate a larger chord of the wing to generate lift, 6 feet, but the low aspect ratio indicates this leads to an increase in drag.

5 Airfoil Selection

Uber argues in their white paper that an aircraft optimized for forward flight will be more efficient than one optimized for hover. Their reasoning is that an urban air taxi will spend more time flying to a

destination than hovering over it. It follows that the airfoil design should be designed for lifting at cruise speed with low drag. The wing does not need to perform well at low speeds since the rotors can generate lift when pointed up. This would indicate that a low amount of camber is needed. However, since the rotors in hover will create a large moment at the root of the wing, a thick airfoil is needed to increase the moment of inertia to resist bending. This is too important to miss, since an undersized airfoil section will lead to an overweight wing that needs thick skins to keep stresses low. As such, the NACA 23018 airfoil was chosen. It has an 18% thickness to chord ratio and was produced on the Cessna 402 shown below.



Figure 4 – Cessna 402

The shape of the 23018 airfoil was plotted in excel and shown in Figure 5 below.

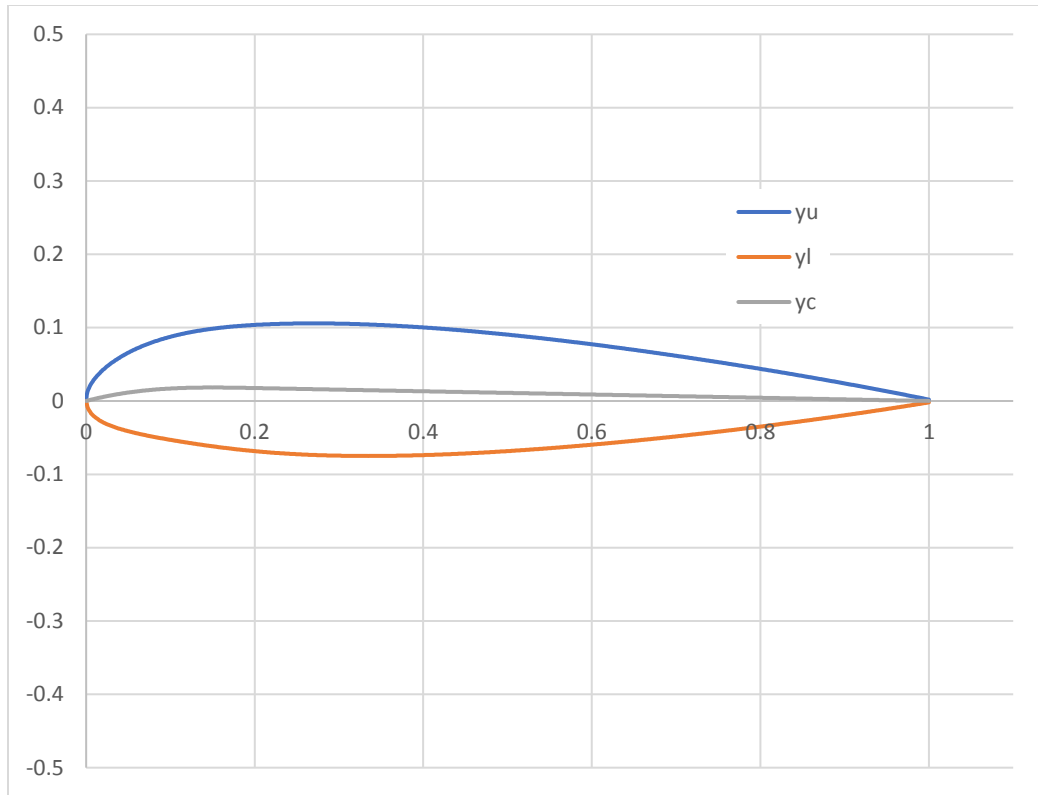


Figure 5 – NACA 23018 Airfoil

XFOIL, a CFD program, was used to determine coefficients of lift, moment and drag. A sample output of XFOIL is shown below in Figure 6.

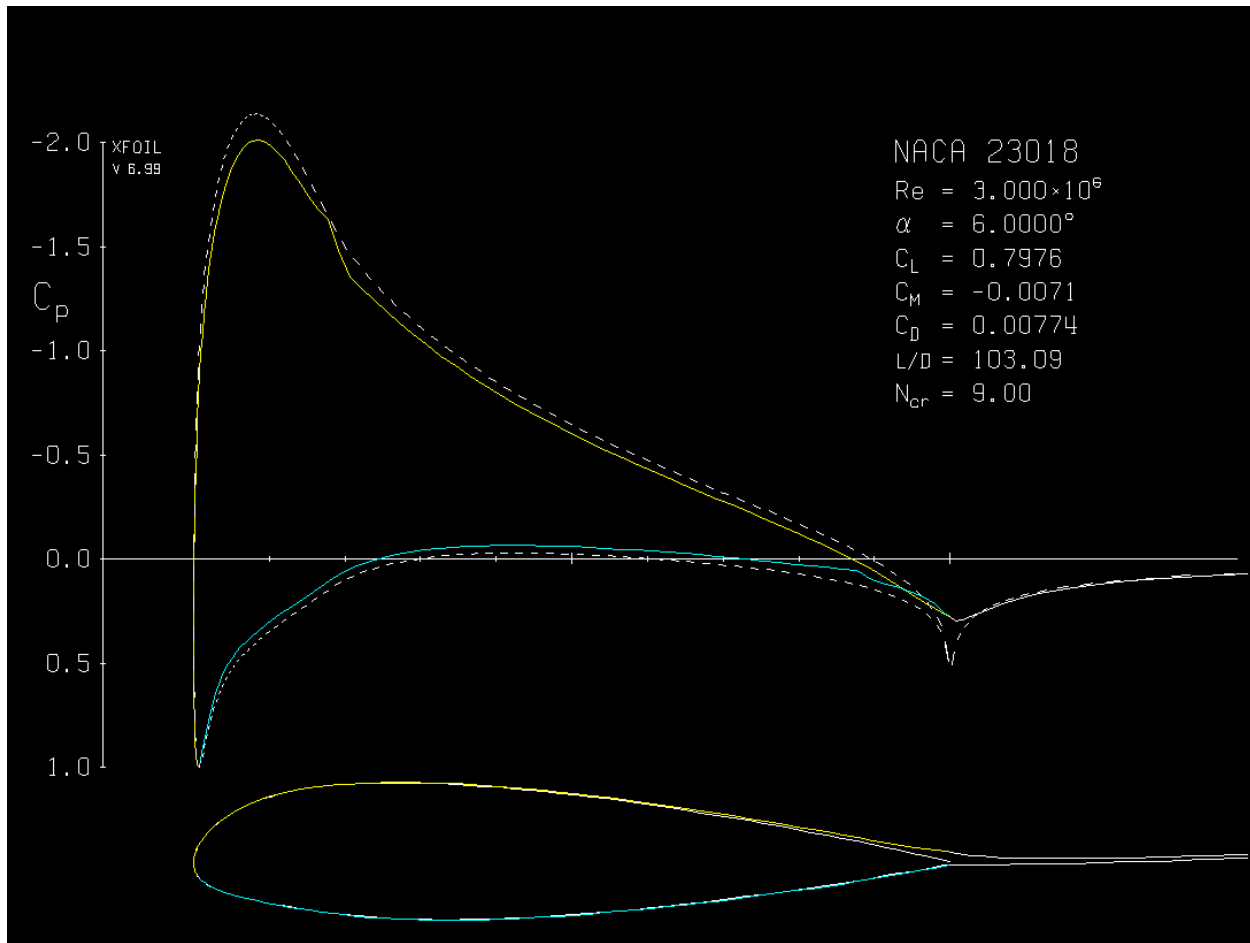


Figure 6 – XFOIL output for NACA 23018, AoA = 6 deg

Reynolds number was calculated using Equation 2,

$$Re = \frac{\rho V l}{\mu} \quad (2)$$

where Re is Reynolds number, ρ is the density of air, V is cruise velocity, l is the length of the chord of the airfoil, and μ is the dynamic viscosity. The Reynolds number was calculated at sea level and again at 8,000 ft using the parameters in Table 2. (11)

Table 1 – Reynold’s Number

	Sea Level	8,000 ft
ρ (slugs/ft ³)	2.38E-03	1.89E-03
μ (slugs/ft s)	3.74E-07	3.57E-07
V (fps)	220	220
l (ft)	6.00	6.00
Re	8.40E+06	6.99E+06

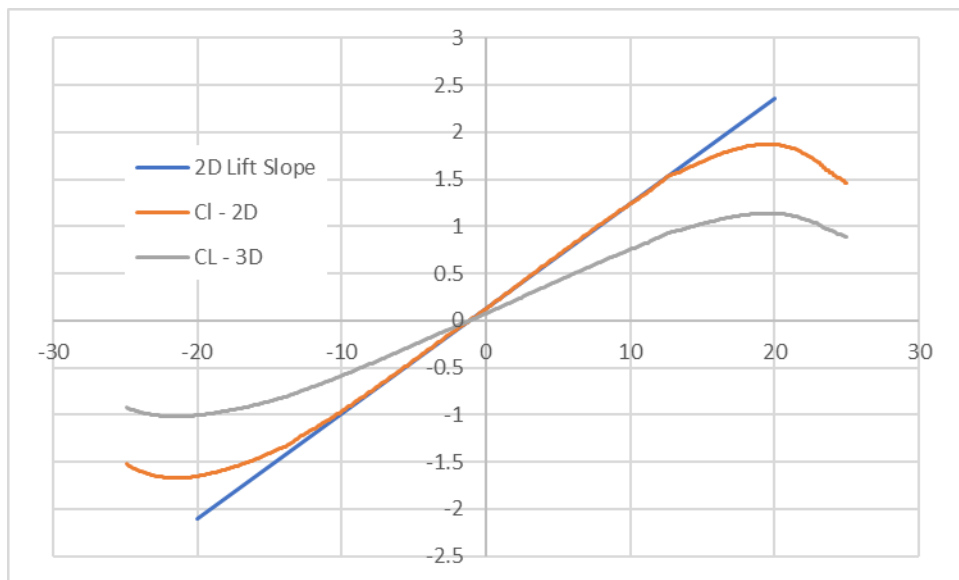
An iteration was run in XFOIL from negative angles of attack to positive, to investigate the lift slope and stall angle of the wing. To account for the loss of lift for a 3D wing, equations 12 and 13 are used. (12)

$$C_L = \frac{a}{a_0} C_l \quad (2)$$

$$a = \frac{a_0}{\left(1 + \frac{a_0}{AR\pi e}\right)} \quad (3)$$

where C_L is the 3D coefficient of lift, C_l is the 2D Coefficient of lift, a is the 3D lift slope, a_0 is the 2D lift slope, AR is the aspect ratio of the wing, and e is the Oswald efficiency factor.

The results at sea level are shown in Figure 7 and at altitude in Figure 8.

**Figure 7 – NACA 23018 Lift Slope at Sea Level**

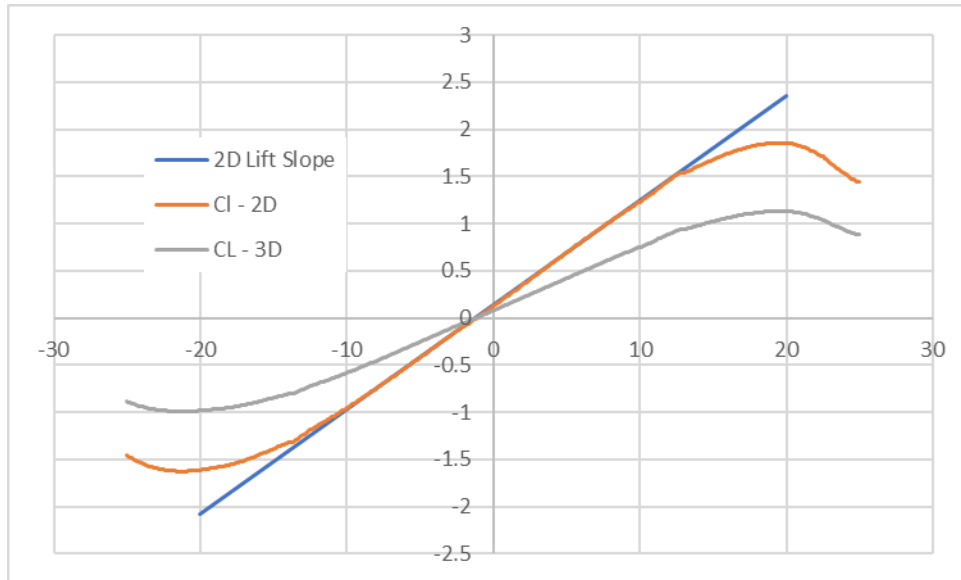


Figure 8 – NACA 23018 Lift Slope at 8,000 ft

The max and min lift coefficients in the graph are used to designate the onset of stall, while the linear portion is used to determine the lift slope. A least squares regression was used for the data between -5 and 5 degrees to determine the lift slope. The data for both sea level and at the aircraft's ceiling limit is shown in Table 3.

Table 2 – 2D and 3D Airfoil Data

	Sea Level	8,000 ft
Re	8.40E+06	6.99E+06
Cl min	-1.77	-1.73
Cl max	1.91	1.90
Lift Slope (2D)	6.48	6.45
CL min	-1.07	-1.05
CL max	1.16	1.15
Lift Slope (3D)	3.92	3.91

6 Wing Redesign

The desire to decrease the moment generated by the rotors lead to the decision of a short, stocky wing. The increase in drag was thought to be worth it, since the engines that were designed to lift the entire aircraft would be able to produce enough thrust to overcome it. However, the large aspect ratio also caused a decrease in the 3d lift coefficient. The short, stocky wing let almost half of its theoretical lift spill over the edge of the wing. The stall speed of this initial design was shown to be over 65 knots. For comparison, the Cessna 172 has a stall speed of around 40 knots with flaps deployed. Since flaps were not used in the shape of the airfoil in the calculation of the stall speed of the tiltrotor, a direct comparison is not possible. However, the stall speed was too high for an aircraft that would be working in an urban, commuter environment. The aircraft would need to be able to transition its rotors and fly safely at slower speeds. The stall speed was calculated using equation 4 below. (12)

$$C_L = \frac{L}{\frac{1}{2}\rho V^2 S} \quad (4)$$

Where L is the lift generated by the wings, V is the velocity of the aircraft, and S is the planform area of the wing. A new approach was taken. The stall speed was calculated at altitude, setting L to the weight of the aircraft and C_L to its max value from table 3. A new solution was implemented to increase the aspect ratio of the wing, but without giving up the desire to decrease the moment at the root of the wing. The wing would be lengthened to 18 feet and the chord shortened to 4 feet, increasing the aspect ratio from 4 to 9. A wing strut would be added that extended from the aircraft fuselage and attached to the wing 6 feet from the root. An example of this design is shown in the silhouette of the Cessna 172 Skyhawk in Figure 9.

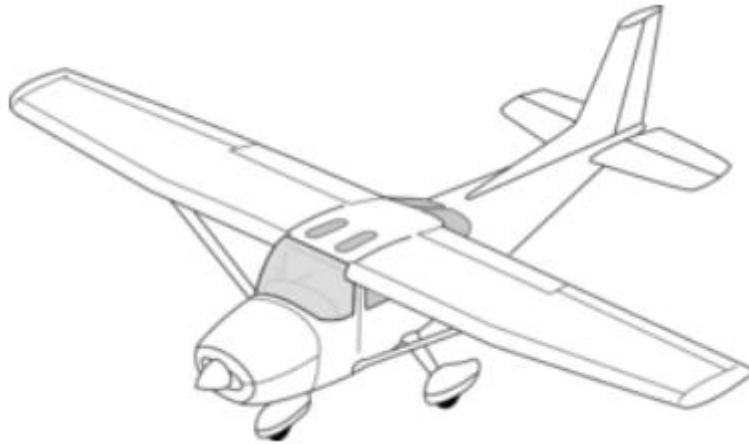


Figure 9 – Cessna 172 Skyhawk Silhouette

This change is reflected in the updated figures and tables below. In figure 10, the now more slender wing layout is shown, with the 6-foot dimension indicating where the wing strut will attach to a rib.

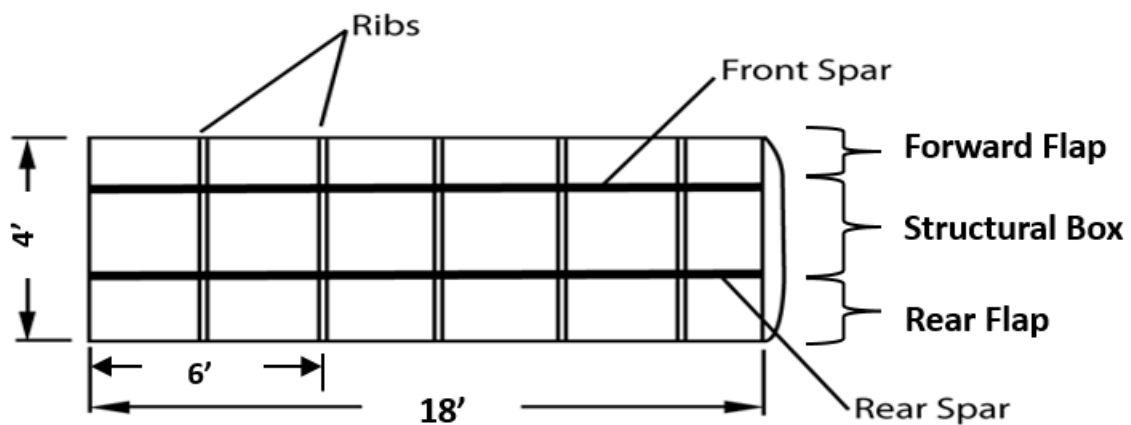


Figure 10 – Wing Layout [Redesign]

The Reynolds number was recalculated using equation 2 since the chord length had shortened. The values are presented in table 3.

Table 3 – Reynolds Number [Redesign]

	Sea Level	8,000 ft
ρ (slugs/ft ³)	2.38E-03	1.89E-03
μ (slugs/ft s)	3.74E-07	3.57E-07
V (fps)	220	220
l (ft)	4.00	4.00
Re	5.60E+06	4.66E+06

The new Reynolds number caused a change in the 2D airfoil data and the increase in aspect ratio changed the 3D wing data further. Figures 11 and 12 show the new lift slopes.

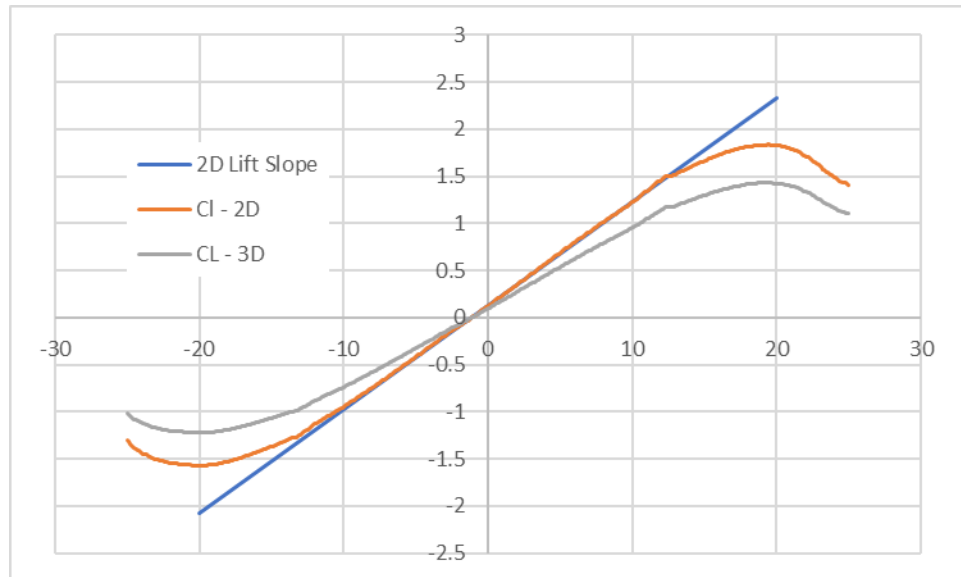


Figure 11 – NACA 23018 Lift Slope at Sea Level [Redesign]

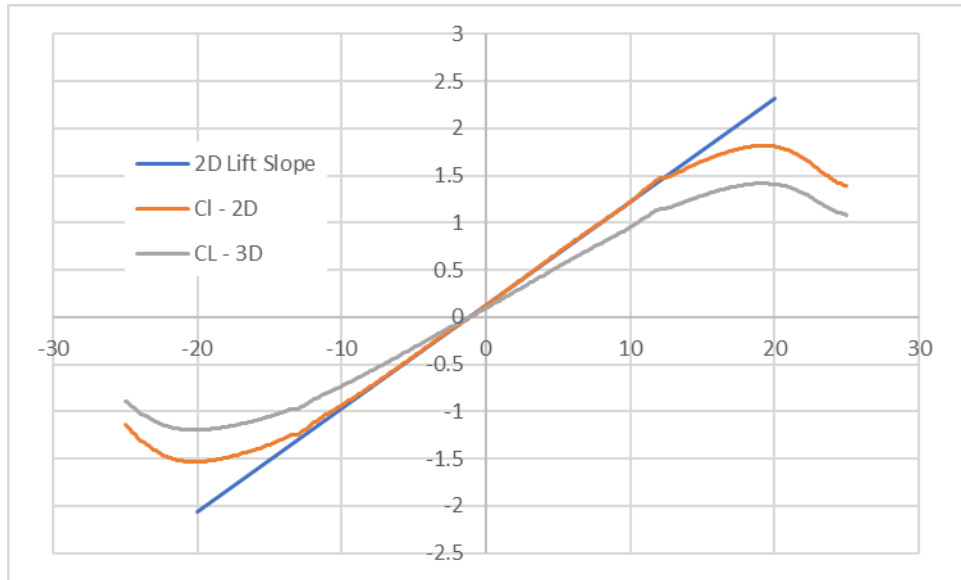


Figure 12 – NACA 23018 Lift Slope at Altitude [Redesign]

The data for both the original and redesign are compiled in Table 4. The new stall speed is now less than 60 knots.

Table 4 – 2D and 3D Airfoil Data [Redesign]

	Original Design		Redesign	
	Sea Level	8,000 ft	Sea Level	8,000 ft
Re	8.40E+06	6.99E+06	5.60E+06	4.66E+06
Cl min	-1.77	-1.73	-1.69	-1.66
Cl max	1.91	1.90	1.88	1.87
Lift Slope (2D)	6.48	6.45	6.41	6.38
CL min	-1.07	-1.05	-1.32	-1.29
CL max	1.16	1.15	1.46	1.45
Lift Slope (3D)	3.92	3.91	4.98	4.96

7 Load Cases

The initial sizing of the wing starts with the weight of the aircraft that the wing must bear in flight, which will be assumed to be 2000 lbs. This is between the maximum gross weights of the Cessna 152 and Robinson R44. The rough breakdown of weight in an electrical configuration was assumed to be 500 lbs of battery/fuel, 200 lbs for two motors, 400 lbs for pilot and passenger, 800 lbs of airframe/wing structure, and 100 lbs of avionics/other systems. The design will consider all the weight of the batteries/fuel to be in the wing structure.

7.1 Hover/Takeoff

The first load case considered was the hover/take off condition, shown in Figure 3. The aircraft positions it's rotors up, the blades providing lift and carrying the weight of the aircraft. If the aircraft CG is offset, this must be balanced by inducing a moment in the rotors

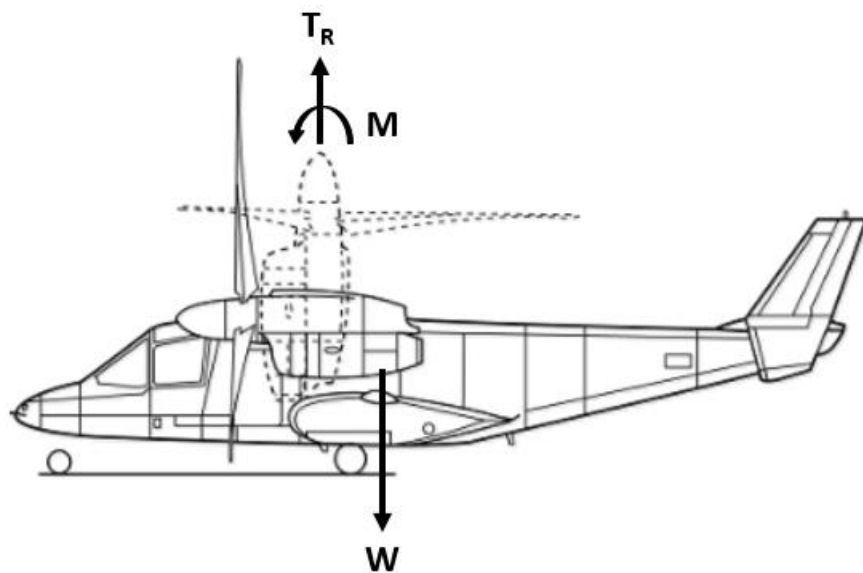


Figure 13 – Hover/Take-Off Load Case Free Body Diagram

The force and moment balance is given below in equations 2 and 3.

$$T_R = nW \quad (5)$$

$$M = nWe \quad (6)$$

Where T_R and M are the necessary thrust and moment produced by the rotors and swashplate, n is the load factor, W is the weight of the aircraft, and e is the eccentricity or distance between the center of lift and center of gravity. Since the weight of the motors and fuel are at the same station line as the wing, the eccentricity can be designed to be small, varying between 0 and 6 inches depending on the cargo. If the eccentricity is larger than 6 inches, the aircraft will simply “lean back” until the CG is closer in line with the thrust vector. Part 27 of the Code of Federal Regulations (CFR) for normal category rotorcraft requires structure to hand between -0.5 and 2.0 G limit loading under requirement 27.337b (09). This is less stringent than 27.337a requirement of -1 to 3.5 Gs, but it would be impossible for a typical rotor system to generate that amount of thrust in a fully loaded take-off, so the smaller requirements are still conservative. The free body diagram from the front view is shown in Figure 14, with actual values. Figure 15 shows the free body diagram for one wing only.

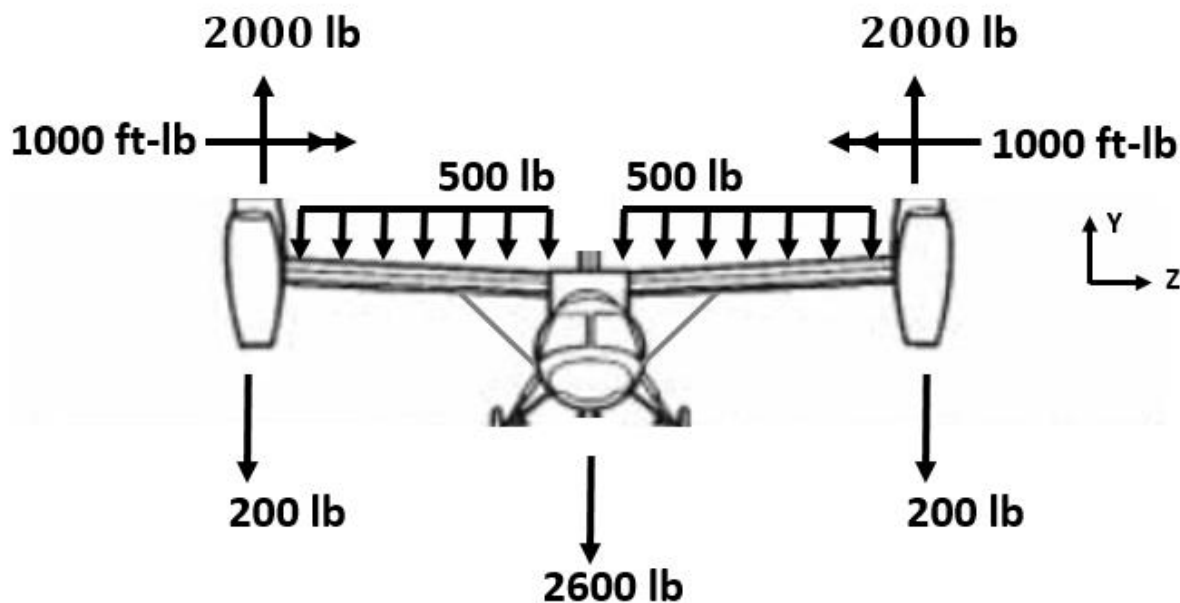


Figure 14 – Free Body Diagram for Takeoff/Landing – Front View

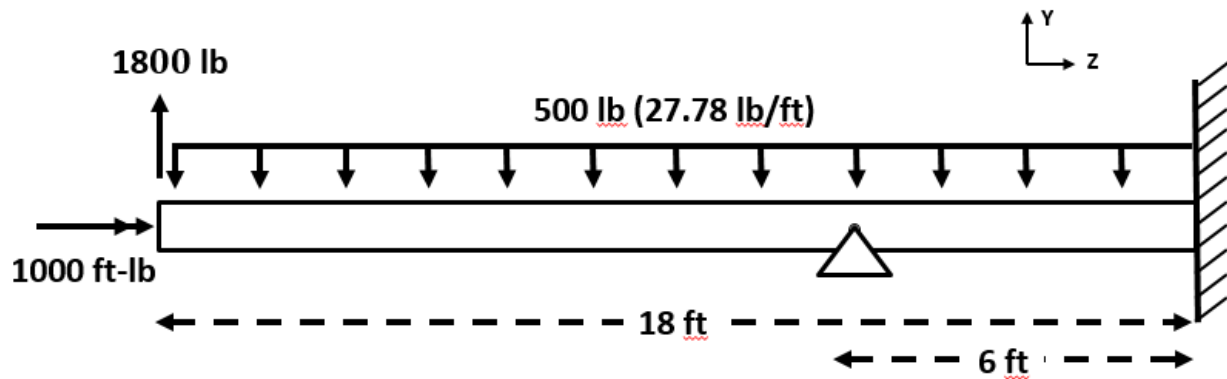


Figure 15 – Free Body Diagram for Takeoff/Landing – Wing Only

During a hover or takeoff maneuver, the downwash of the rotors would impinge on the wing of the aircraft. The lift generated over that section would be negated as the rotor thrust is cancelled by the air pushing down on the wing. More power is supplied to the rotors to overcome the downwash, pushing harder on the wing. The overall lift generated by the rotor wing system still must be equivalent to the weight of the aircraft showing that downwash is a local event only and can be ignored as you move away from the wing tips. This can be visualized in Figure 14 where both the upward and downward force on the tip of the wing increase an equivalent amount and therefore have no effect on the wing load analysis shown in Figure 15. The max stresses of a wing occur at the root, so rotor downwash is ignored in the structural analysis of this report.

7.2 Hard Landing

In a hard landing condition, the wing is stressed from reacting the inertia of the rotor and energy/propulsion systems coming to a rest. A wing at rest is generating 0 G's of upward thrust and therefore must react the weight of the systems it carries. The hard landing condition considered will be negative 1 G's meaning the wing will react double the weight it typically experiences while sitting in the hangar (09).

7.3 Transitional

After the aircraft successfully takes off and hovers, it will transition into forward flight. A 45 degree rotor tilt will be considered for the transition. As the rotors begin to tilt forward, the vehicle moves forward. Airflow over the wings and horizontal stabilizer start to generate lift and the fuselage develops drag. Figure 4 below shows the free body diagram.

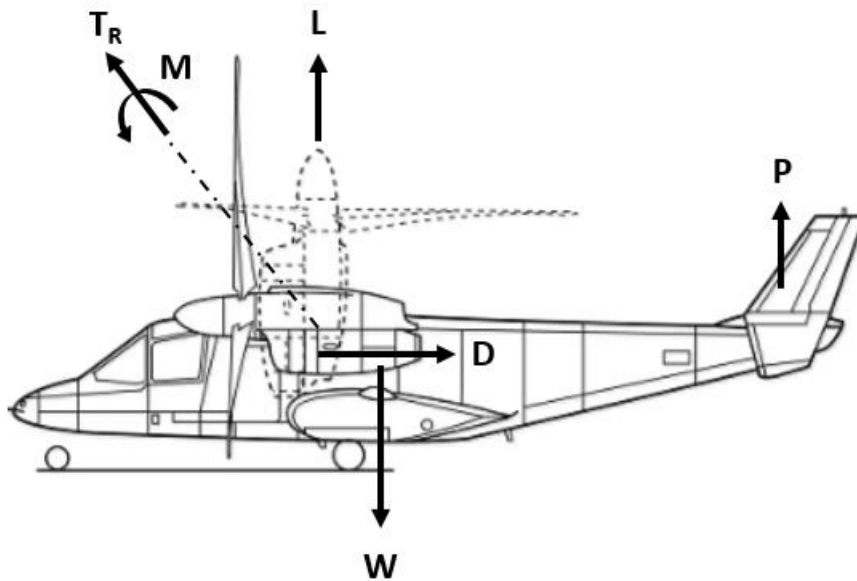


Figure 16 – 45° Transition to Forward Flight Load Case

It can be seen from Figure 4 that the weight of the aircraft is buoyed from both the wings and the rotors in this transitional condition. The rotors need to generate less moment as the horizontal stabilizer begins to balance the aircraft with the efficiency of the tail boom acting as a large lever arm. To simplify calculations, the moment generated in the transitional load case will be assumed to be zero. The sum of forces are shown in equations 7 and 8 below

$$T_R \cos 45^\circ + L = nW \quad (7)$$

$$T_R \sin 45^\circ = D \quad (8)$$

The only new variables for this load case are L, the lift generated by the wings, and D, the drag induced by the fuselage. The transitional load case will be assumed to take place at the stall speed of 60 knots, or 100 feet per second.

7.4 Steady Flight and Rapid Pull Up from a Dive

The rotors will continue to tilt forward until steady level flight is achieved. The free body diagrams for steady flight and a rapid pull up from a dive are shown in Figures 17 and 18 below.

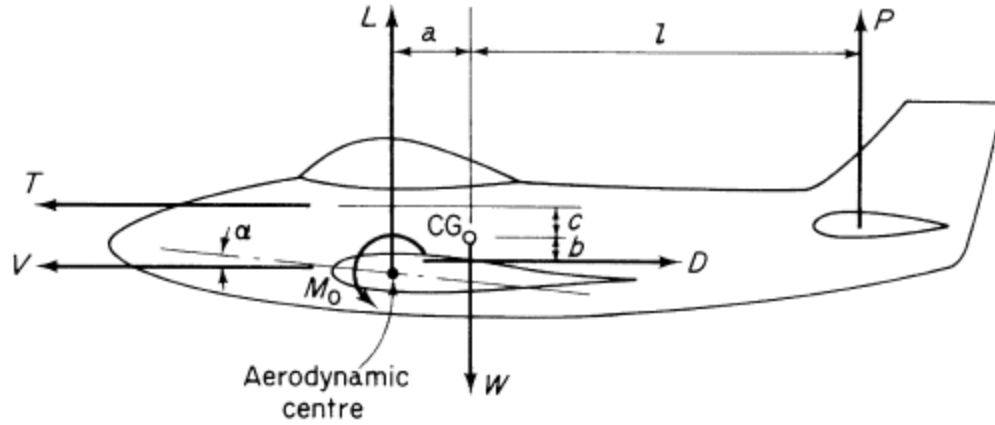


Figure 17 – Steady Level Flight

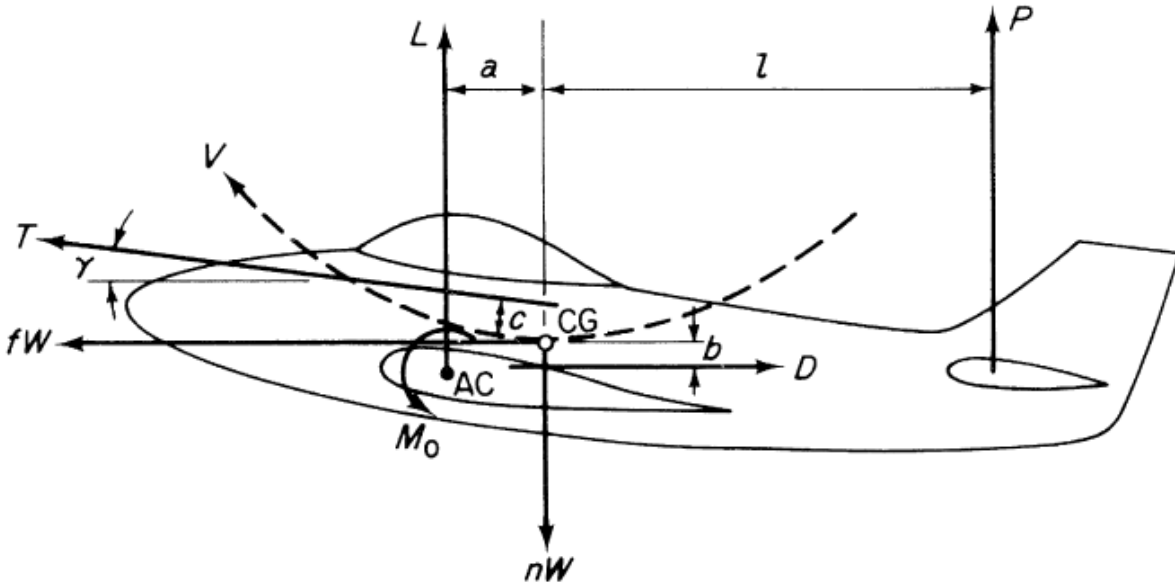


Figure 18 – Rapid Pull Up from Dive

Although the aircraft's lift is no longer generated by the rotors but instead by the wings, the principle of equation 5 still applies. The lift must be equal to the weight multiplied by a load factor. This can be combined with the aerodynamic theory presented in equation 9 to form the stall envelope defined in equation 10 below.

$$L = \frac{1}{2} \rho S C_{L,max} V^2 \quad (9)$$

$$n_{stall} = \frac{\rho S C_{L,max}}{2W} V^2 \quad (10)$$

Once in level flight, the regulations of Part 23 for normal category aircraft apply. The aircraft is no longer limited to the 2 or 3.5 G limits of §27.337. In §23.333 and §23.337, the CFR requires the aircraft to be restricted to a positive normal load factor of 4.4 and a negative normal load factor of -1.76 at cruise and -1 at dive (03). These requirements, combined with the stall curve, create the maneuvering envelope.

7.5 Gust Loads

In §23.333 and §23.341, the CFR also requires the structure to be able to withstand gust loads. Gust loads are specified to be 50 ft/s at cruise and then varying linearly to 25 ft/s at dive (03). The load factor given in CFR is shown in Equations 11 through 13

$$n_{gust} = 1 + \frac{K_g U_{de} V a}{498(\frac{W}{S})} \quad (11)$$

$$K_g = \frac{0.88\mu_g}{5.3 + \mu_g} \quad (12)$$

$$\mu_g = \frac{2 \frac{W}{S}}{\rho C a g} \quad (13)$$

In Equation 11, n_{gust} is the normal load factor due to gust, K_g the gust alleviation factor, U_{de} is the gust velocity, V is the velocity of the aircraft, a is the lift slope of the wing, W is the weight of the wing, S is the surface area of the wing, μ_g is the airplane mass ratio, ρ is the density of air, and g is the acceleration due to gravity. All variables have units in slugs, feet, and seconds except for velocity which is in knots.

With both the maneuver and gust envelopes defined, the allowable envelope can be defined, shown for both sea level and 8,000 ft in figures 19 and 20 below.

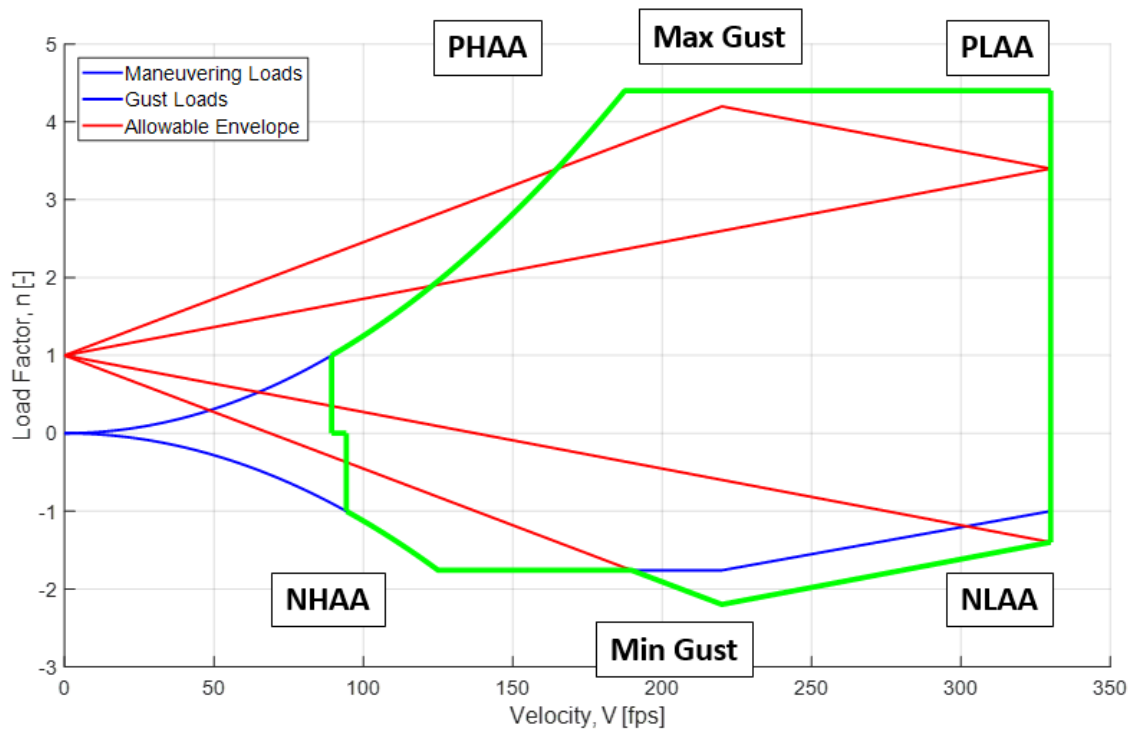


Figure 19 – V-n Diagram for Sea Level

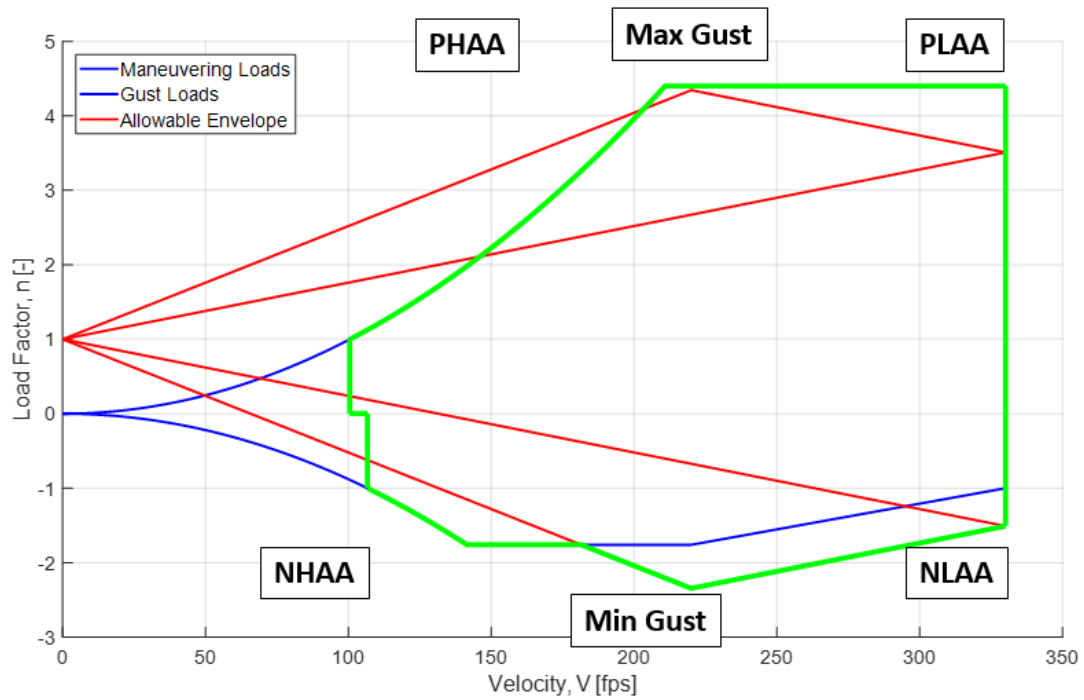


Figure 20 – V-n Diagram for 8,000 feet

The allowable envelope begins when the aircraft can maneuver above 1g, indicating the point where the aircraft is in steady forward flight. The allowable envelope continues along the positive and negative stall curve until it reaches the max and min maneuver limit given in the CFR. This point is called positive high angle of attack (PHAA) and negative high angle of attack (NHAA). These points describe the load case where the aircraft is pulling the maximum allowable load at the slowest possible speed, with the wing at an angle of attack that would stall the airplane. Similarly, positive low angle of attack (PLAA) and negative low angle of attack (NLAA) are load cases at the highest speed where lower angles of attack result in high normal loading on the wing. While the normal load is the same between the PHAA and PLAA load cases, the drag and deflections will be different due to the difference in speed and angle of attack. Thus it is important to treat these as separate load cases. Between the high and low angle of attack load cases, the max and min gust cases are critical at cruise velocity. All load cases are analyzed at sea level and again at 8,000 ft. The max gust case will be assumed to have a normal load factor of 4.4, which is conservative according to figures 19 and 20.

The wing is sized to the 16 load cases shown in table 5 below.

Table 5 – Critical Load Cases

Load Case		Velocity (fps)	Re	AoA (°)	N	Cl	Cd	Cm
LC1 Hard Landing		0	0	0	-1	0	0	0
LC2 Take off/Hover		0	0	0	2	0	0	0
Sea level	LC3 45° flight	100	2.55E+06	6.6	2	0.88	.0072	.010
	LC4 PHAA	188	4.79E+06	18.7	4.4	1.87	.028	.020
	LC5 PLAA	330	8.40E+06	4.1	4.4	0.60	.0066	.009
	LC6 NHAA	125	3.18E+06	-21.4	-1.8	-1.69	.047	.053
	LC7 NLAA	330	8.40E+06	-3.0	-1.4	-0.2	.008	.011
	LC8 Max Gust	220	5.60E+06	0	4.4	0.13	.006	.008
	LC9 Min Gust	220	5.60E+06	0	-2.1	0.13	.006	.008
8,000 ft	LC10 45° flight	100	2.12E+06	8.7	2	0.86	.008	.009
	LC11 PHAA	211	4.47E+06	19.8	4.4	1.87	.038	.022
	LC12 PLAA	330	6.99E+06	5.6	4.4	0.76	.007	.009
	LC13 NHAA	142	3.01E+06	-21.3	-1.8	-1.66	.050	.053
	LC14 NLAA	330	6.99E+06	-3.6	-1.5	-0.26	.008	.011
	LC15 Max Gust	220	4.66E+06	0	4.4	.13	.006	.008
	LC16 Min Gust	220	4.66E+06	0	-2.3	.13	.006	.008

8 Strut Design

The wing acts a cantilevered beam on the x-z plane (fore-aft loading) and as a cantilevered beam with a simple support at the wing strut attachment point on the y-z plane (up and down loading, shown in Figure 15). The reactions on the x-z plane can be solved for by a simple sum of forces and moments. The reactions of the y-z plane must be solved for using the method of superposition. The generic free body diagram is shown below in Figure 21, replacing the simple support with a supporting load.

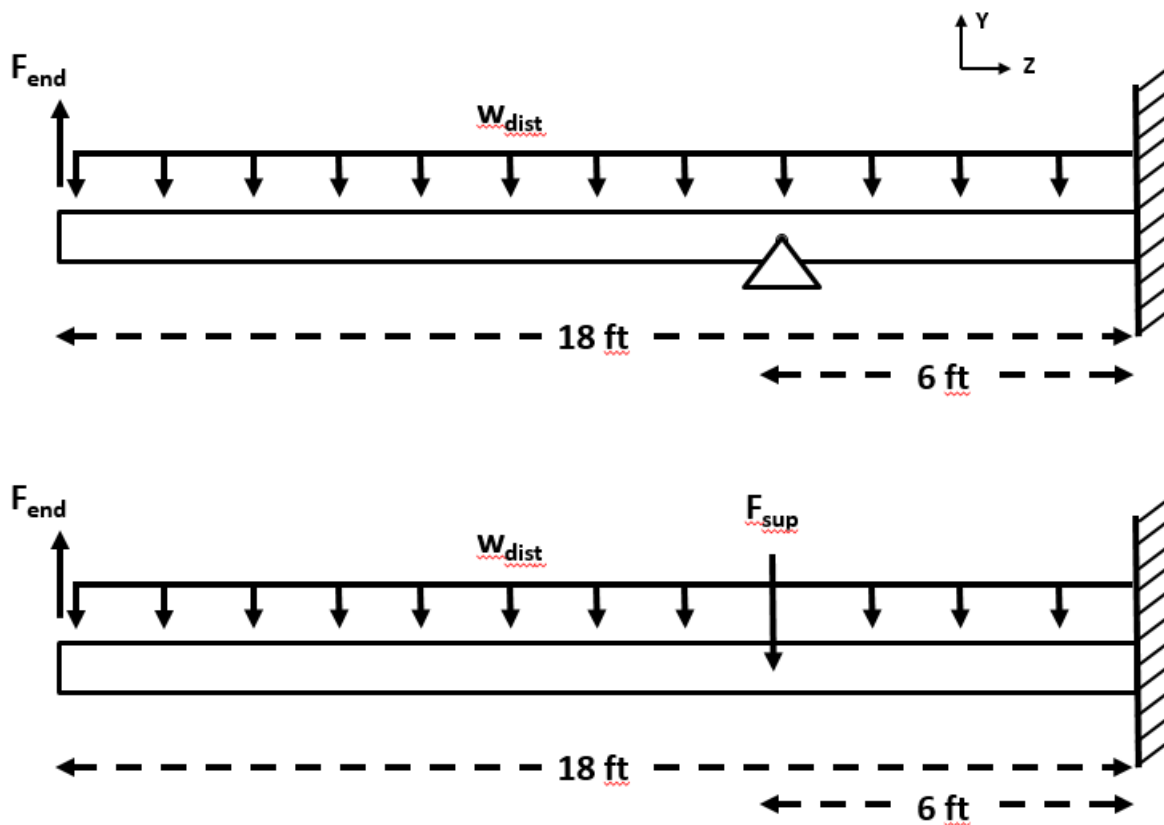


Figure 21 – Cantilevered Beam with Simple Support

The method of superposition allows for each of the three loadings to be applied separately and their shears, moments, and deflections may be summed for the true solution. The deflection of the beam at the supporting load can be set to zero, modeling a simple support and allowing for the reaction to be solved. The equations are shown below. (13)

$$[\text{Deflection due to } F_{end}] \quad y_{sup} = 288 \frac{F_{end}}{EI} \quad (14)$$

$$[\text{Deflection due to } w_{dist}] \quad y_{sup} = -129 \frac{w_{dist}(18)}{EI} \quad (15)$$

$$[\text{Deflection due to } F_{sup}] \quad y_{sup} = -72 \frac{F_{sup}}{EI} \quad (16)$$

$$[\text{Sum of deflections set to 0, solve for } F_{supp}] \quad F_{supp} = 24F_{end} - 10.75(18w_{dist}) \quad (17)$$

F_{end} , w_{dist} , and F_{sup} correspond to the forces shown in Figure 21. y_{sup} is the displacement at the support load, E is the modulus of the beam, and I is its moment of inertia. Plugging in the values from Figure 15 into equation 17 gives a support load of over 6,000 lbs, more than the weight of the aircraft! The simple support is acting like an infinitely stiff fulcrum which has a prying effect on the fixed end of the beam. The tip load is being multiplied since it is now performing as a crow bar with a large lever arm to act upon. These assumptions do an adequate job modeling the behavior of a wing and strut. Further refinement can be found by introducing flexibility to the joint and allowing it to move along with the wing. Equation 16 can be rewritten into Equation 18 shown below to model the stiffness of the strut, k_{sup} . The sum of the deflections no longer equal zero, but they can be multiplied by the stiffness of the support to solve for the reaction load.

$$y_{sup} = -12 \frac{k_{sup} y_{sup}}{EI} \quad (18)$$

$$F_{supp} = \frac{k_{sup}}{EI + 12k_{sup}} (288F_{end} - 129(18 w_{dist})) \quad (19)$$

It is important that all units must be in pounds and feet for the constants in equation 19 to be applicable. We know from equation 17 that as the stiffness approaches infinity, the supporting load approaches 6,000 lbs. As the stiffness approaches zero, the reaction load approaches 0. The flexibility of the joint now controls the reactions that will be present and can be optimized to minimize the stresses of the wing.

9 Analysis

Analysis of the structure was performed in MatLab. For each load case, each individual load on the beam was summed for the total distributed load on the beam. This included the force of the rotors in the x and

y direction, the lift of the wing, the drag of the wing, and the weight of the components being carried by the wing. The distributed load in the y direction is shown for LC3, 45deg flight, in Figure 22. LC3 is the best load case to demonstrate the analysis because it displays the effects of the rotor in the x and y direction as well as the effects of the wing. The results from other selected load cases are shown in the Appendix.

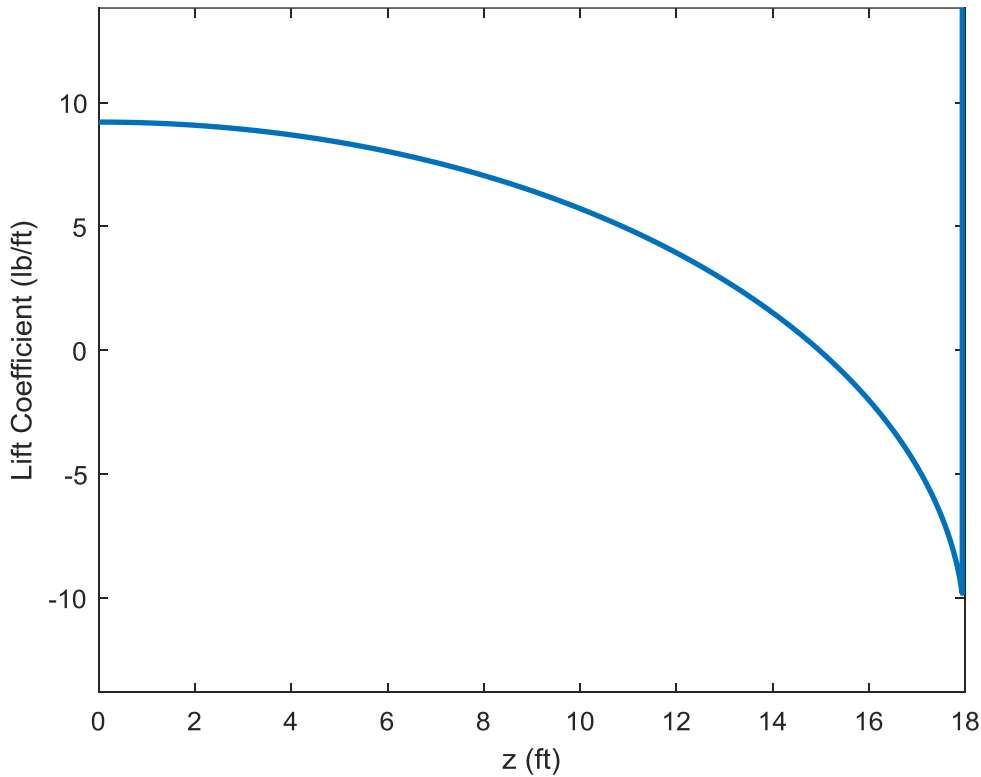


Figure 22 – LC3 45deg Flight Y-Load Distribution

The lift distribution was assumed to be the average of an elliptical and rectangular distribution, reaching the highest amount of lift at the root of the wing (the left end of the graph.) This is shown in equation 20..

$$l(z) = \frac{L}{2b} + \frac{L}{4b\pi} \sqrt{1 - \frac{z^2}{b^2}} \quad (20)$$

The weight of the batteries, which is spread across the full span of the wing, is then subtracted from the lift causing the distribution to be negative at the tip (the right side of the graph) where the lift was lowest. The maneuver is only at 100 fps, so the wing is not able to carry the entire weight of the aircraft in the 2 G maneuver. The lift from the rotors carries the remaining load and is shown at the far right of the graph.

The point load is spread over a very small length of the span making a large distributed load that runs well above the top of the graph. The X distributed load is set up in a similar way and is shown in Figure 23

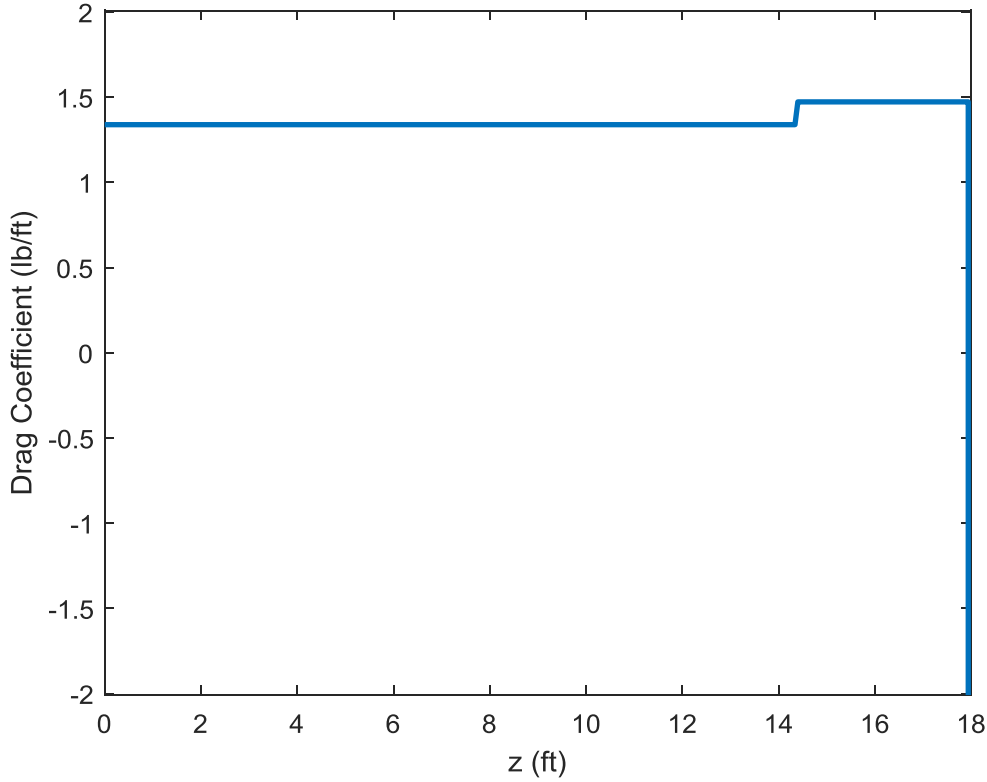


Figure 23 – LC3 45deg Flight X-Load Distribution

In the x direction, the wing does not have to react to any weight of its components. There is a distributed load due to drag, which increases by 10 percent over 20% of the span closest to the tip. This is to account for higher drag at the tip due to vortices. Any drag due to the rotor wash impinging on the wing is assumed to be overcome by the rotor itself, and does not affect the loading on the wing. The drag is calculated by equation 21.

$$D = \frac{1}{2} \rho V^2 S \left(C_d + \frac{C_L^2}{\pi A R e} \right) \quad (21)$$

There is a component of the rotor that acts in the negative x direction, pulling the aircraft forward in flight as the drag of the wing and fuselage try to slow the aircraft down. The forward thrust of the rotor is also

a point load, and is distributed over a small area leading to a value well below the bottom of the chart. When the tilt of the rotors is at 45 degrees, the thrust in the x direction is equivalent to the lift of the rotors in the y direction. However, in pure forward flight with all the lift delivered by the wings, the tiltrotor thrust must be calculated another way. It was assumed that the rotor produced 4 times as much thrust as there was drag on the wing. This means the fuselage produces 3 times the drag that the wings do.

The wing is at an angle of attack to produce the necessary lift at 100 fps, so the x and y distributed loads need to be transformed into a coordinate system appropriate for analysis. Currently, the load is in the global coordinate system where the lift is inline with the force of gravity and the drag is in line with the direction of the upstream airflow. Equations 22 and 23 will transform the load into the airfoil coordinate system where x runs from airfoil nose to tail and y along the airfoil thickness. This is visualized in figure 24.

$$w_x = -l \sin \alpha + d \cos \alpha \quad (22)$$

$$w_y = l \cos \alpha + d \sin \alpha \quad (23)$$

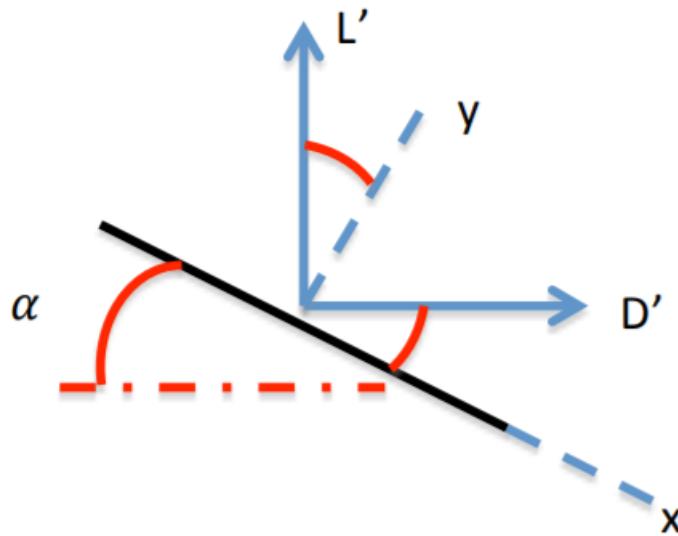


Figure 24 – Coordinate transformation

The load of the strut that is calculated from equation 19 can now be added, since it is also in the airfoil coordinate system. It is calculated in both the x and y direction and has different values for each. Since it

is a point load and spread over a small area, like the weight and thrust of the rotor, its value is off the ends of the chart in figure 24.

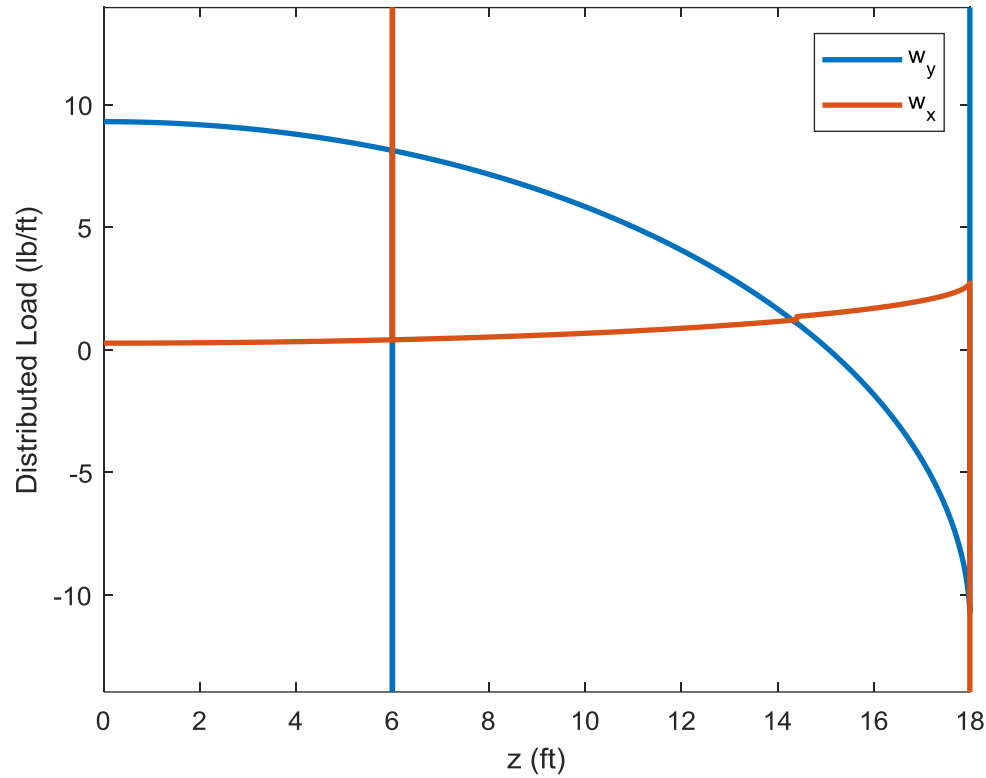


Figure 25 – LC3 45deg Flight

The distributed load can be summed along the length of the wing from the tip to the root, calculating the shear on the wing box in equations 24 and 25 and shown in figure 25

$$S_x = - \int w_x dz \quad (24)$$

$$S_y = - \int w_y dz \quad (25)$$

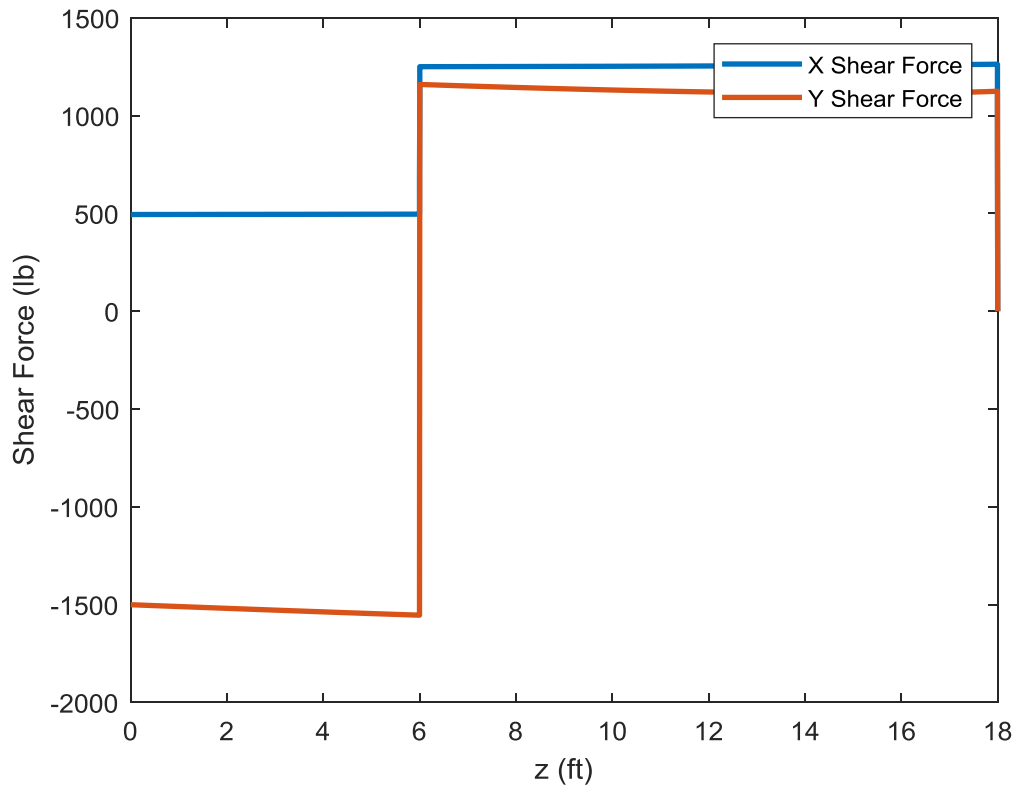


Figure 26 – LC3 45deg Flight Shear Diagram

From the figure, it can be seen the strut at 6 feet has a large effect on the shear than the rotor thrust in the y direction. This is an example of the prying effect discussed in section 8. The critical locations for shear are at the root, just before the strut, just after the strut, and at the tip.

The moments can be calculated by summing the shears from tip to root, shown in equations 26 and 27 as well as figure 26.

$$M_x = \int S_y dz \quad (26)$$

$$M_y = \int S_x dz \quad (27)$$

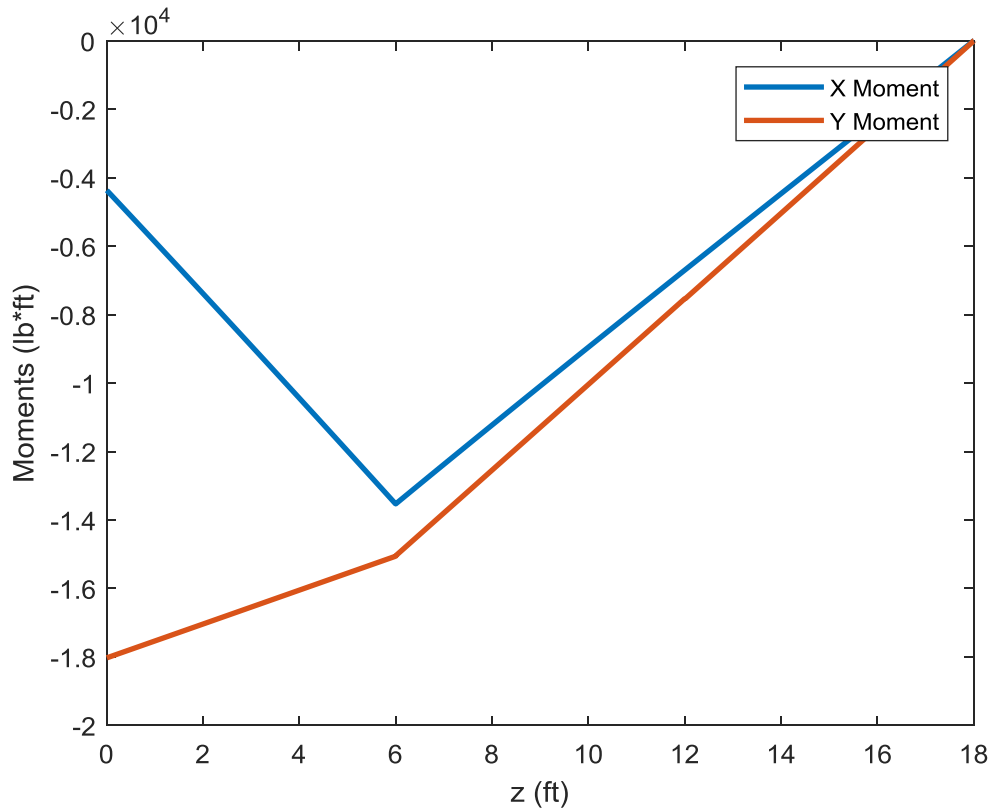


Figure 27 – LC3 45deg Flight Moment Diagram

The strut load in the y direction reverses the moment lowering the load on the root of the wing. This creates two critical locations for moment: at the root and at the strut.

10 Results

Once the forces and moments on the structure were known, the sizing and optimization of the members of the wing could begin. The spar and skin thickness, spar cap and stringer area, and stringer placement were all variables that could be tuned to give a lightweight and efficient structure. The final layout is shown in Figure 27 and Table 6.

Table 6 – Structure Sizing and Material Properties

Material	7050 Al
Skin Thickness	.060 in
Spar Thickness	0.60 in
Cap Area	.01 in ²
Number of Stringers	20
Stringer Area	.0025 in ²
Yield Stress	64 ksi (10)
Modulus	10.5 Msi (10)

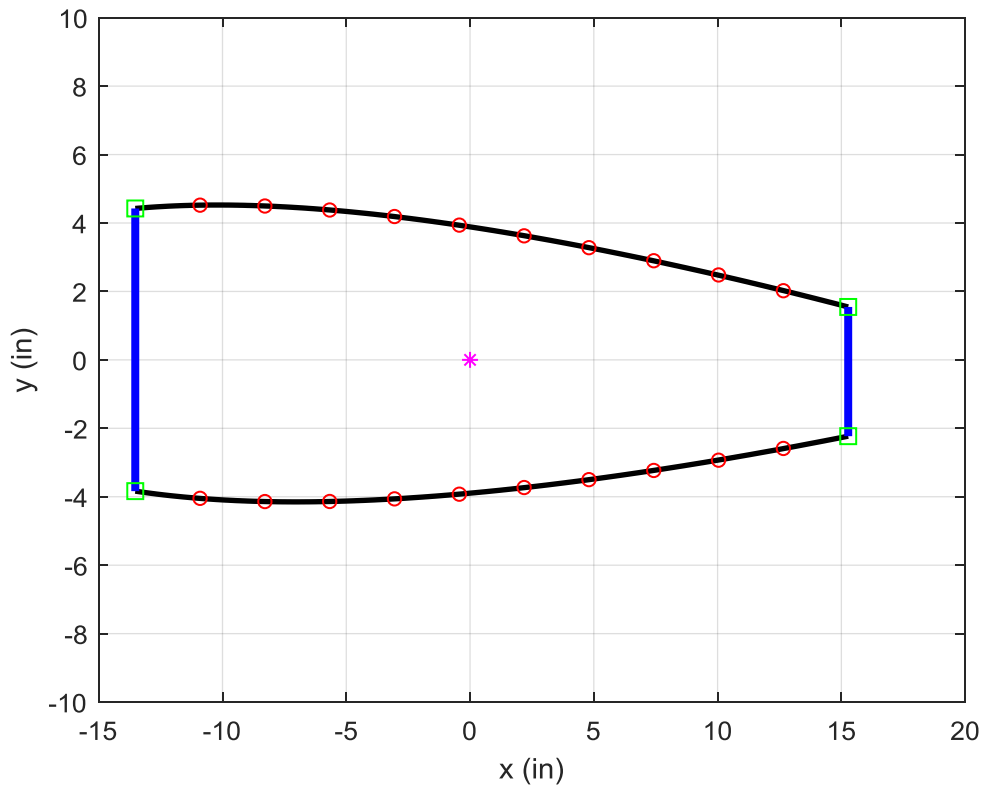


Figure 28 – Wing Box Stringer Placement

The critical load case that sized the components was LC2, Takeoff/Hover. That load case is not the one that puts the most load on the wing, such as LC4 PHAA with a load factor of 4.4. However, LC2 does put the most vertical load at the tip of the wing, creating the largest overturning moment at the strut and root. The diagrams and results of LC2 can be seen in the Appendix.

The inertia of the airfoil was calculated using equations 28 thru 30 below. The equations sum the components of the wing as point masses far away from centroid with low individual inertia about their own center of gravity.

$$I_{xx} = Ay^2 \quad (28)$$

$$I_{yy} = Ax^2 \quad (29)$$

$$I_{xy} = Axy \quad (30)$$

The deflections can be found by summing the moments from root to tip using equations 31 thru 33.

$$u = -K \int \int [-M_x I_{xy} + M_y I_{xx}] dz dz + C_1 z + C_3 \quad (31)$$

$$v = -K \int \int [M_x I_{yy} - M_y I_{xy}] dz dz + C_2 z + C_4 \quad (32)$$

$$K = \frac{1}{E(I_{xx}I_{yy} - I_{xy}^2)} \quad (33)$$

K is an interim calculation involving Young's Modulus, E . u is the deflection in the x direction, v is the deflection in the y direction, and C_1 thru C_4 are constants of integration representing the starting offset and slope. They can be set to zero if the integration is started at the root of the wing and summed to the tip. The results for LC3 are shown in Figure 29.

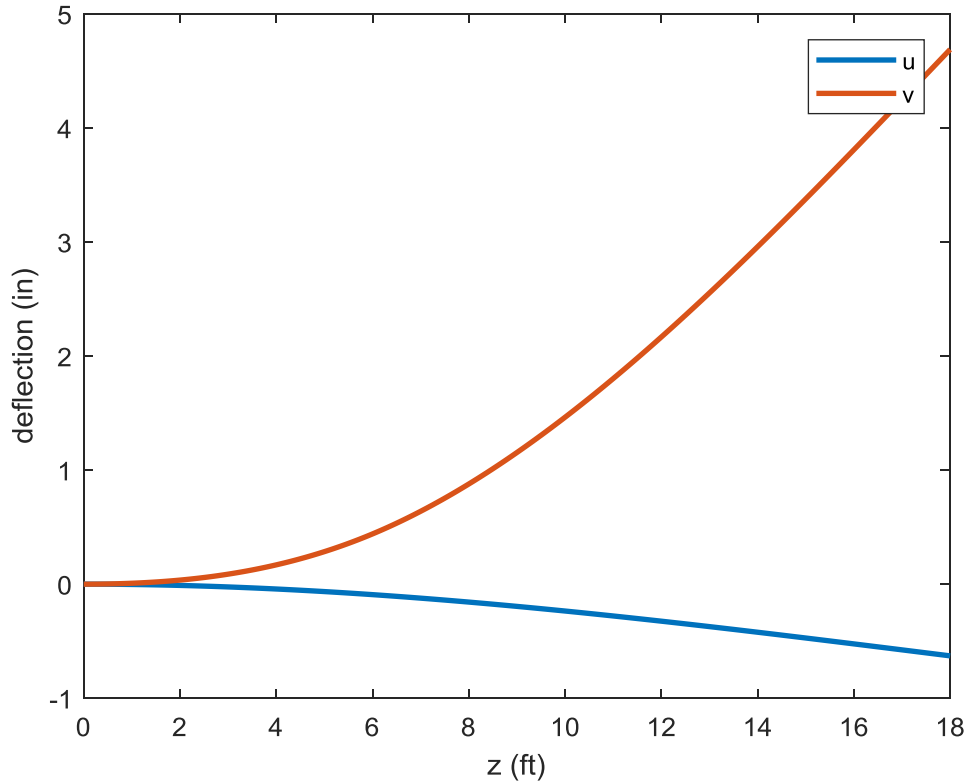


Figure 29 – LC3 45deg Flight, Tip deflection

At the end of the 18 foot span of the wing, the tip deflects almost 5 inches vertically. The rotors also pull it forward almost a full inch. The strut can be viewed as a structural member that is holding the wing back, preventing it from using the full span to build up a large deflection. If the strut had been assumed to be infinitely stiff, also known as a simple support, the deflection would be negative just to the right of the root and then zero at the strut. For the wing to “twist” between the root and the strut would require a large amount of moment. This is a visualization of why the simple support assumption leads to the wing being stressed more than if the strut is flexible and the wing can “breathe”.

The normal stresses in the z direction, σ_{zz} , can be calculated using equation 34.

$$\sigma_{zz} = EK((M_y I_{xx} - M_x I_{xy})x + (M_x I_{yy} - M_y I_{xy})y) \quad (34)$$

Since the only variable that changes along the span of the wing is the moment, the stresses should be checked at the two critical locations. Figure 30 shows the normal stress at the root, and Figure 31 shows the normal stress at the strut.

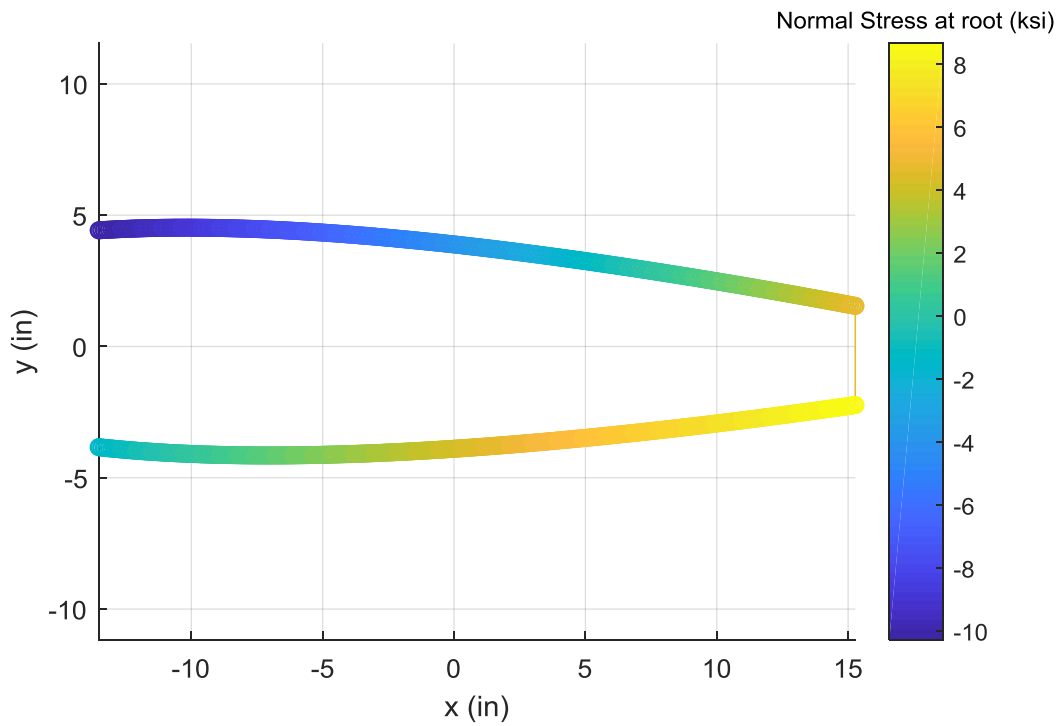


Figure 30 – LC3 45deg Flight Normal Stress at Root

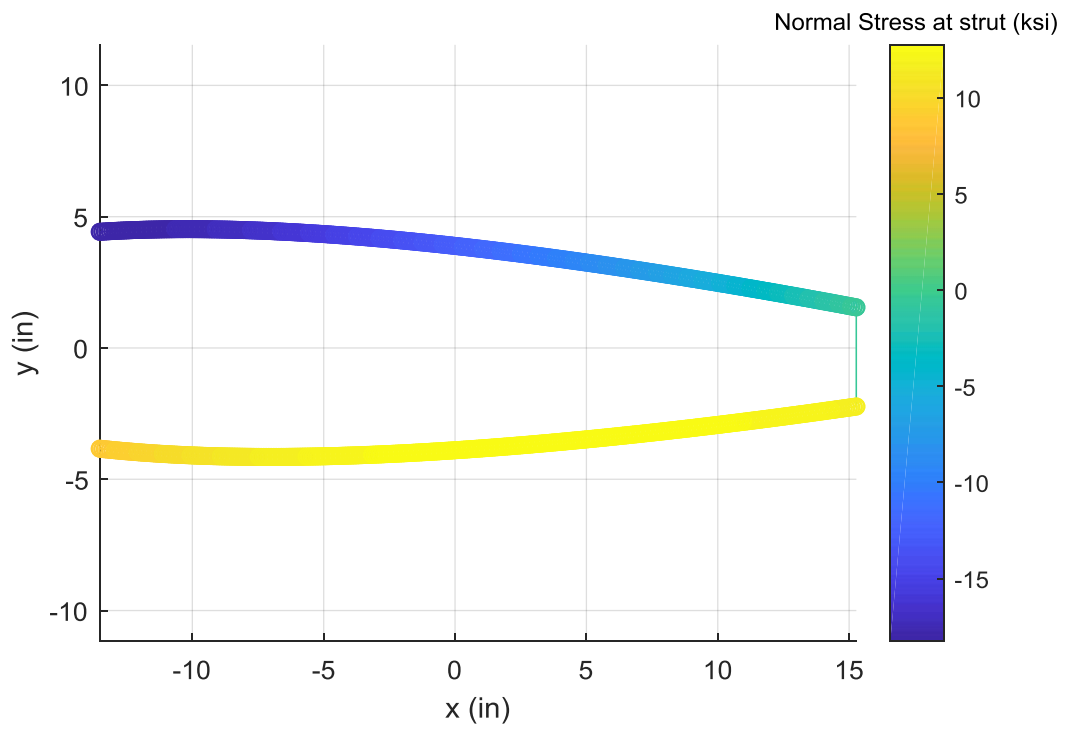


Figure 31 - LC3 45deg Flight Normal Stress at Strut

The normal stress can be visualized over the entire wing, as seen in Figure 32.

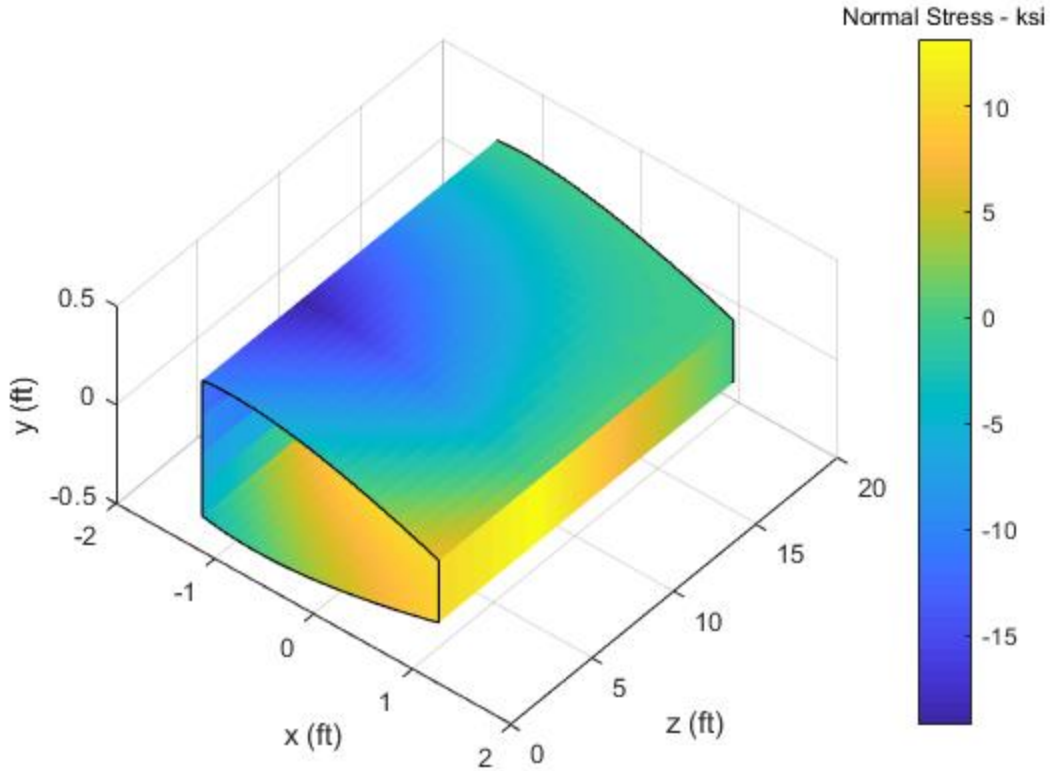


Figure 32 – LC3 45deg Flight Normal Stress

Since the rotor produces forward and upward thrust, it follows that the largest compression would be on the top and forward portion of the wing. The largest tension is on the aft and bottom skin.

The prominent failure mode for skins in compression is not yield but buckling. Buckling is an out of plane deformation of the structural member such that it can no longer support load. Equation 35 was used to find the critical stress, σ_{cr} , at which buckling occurs.

$$\sigma_{cr} = \frac{K\pi^2 E}{12(1-\nu)^2} \left(\frac{t}{b}\right)^2 \quad (35)$$

Where K is a constant that is a function of geometry, conservatively assumed to be 4, E is the modulus, ν is the poisson's ratio, t is the thickness of the skin, and b is the distance between stringers. The margin of safety is calculated using equation 36.

$$MS = \frac{\sigma_{cr}}{\sigma_{zz}} - 1 \quad (36)$$

The rib spacing, shown in Figure 1, was determined by a column buckling check on the stringers. This is conservative since the stringers are supported by skin along their length. A flange buckling check could be performed in the future to reduce weight by increasing the distance between ribs therefor reducing the total number of ribs. Equation 37 is used to solve for the critical load, P_{cr} , in a column at the onset of classical Euler buckling.

$$P_{cr} = \frac{\pi^2 EI}{l_e^2} \quad (37)$$

Where I is the inertia of the stringer and l_e is the effective length of the column. The stringers were assumed to be pinned at either end, so the effective length is equal to the rib spacing. The load in the stringer was solved for using the maximum compressive stress in the stringers times the area of the stringer. Once the rib closest to the root of the wing was placed, a new maximum compressive stress was found in the remaining wing structure and the next rib was placed. This was done for the entire length of the wing.

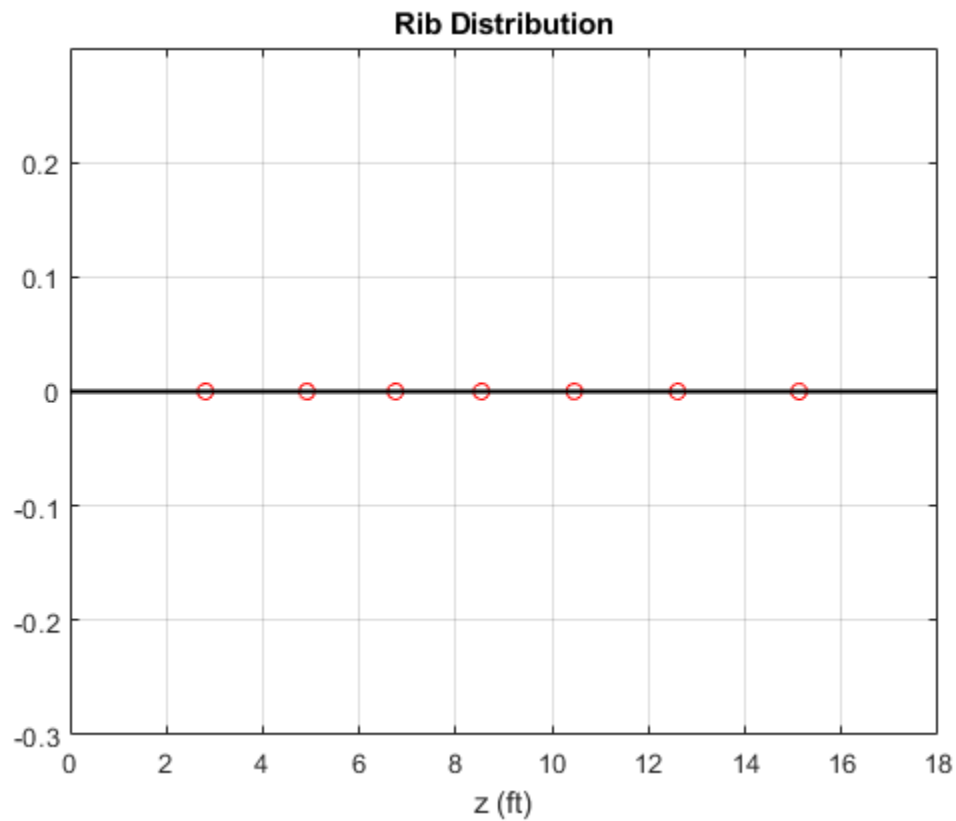


Figure 33 – LC2 Takeoff/Hover Rib Distribution

The rib spacing is slightly more dense around the strut where the normal loads are highest.

The shear is calculated using a boom and panel method, where the area of the skin and spars are lumped with the stringers and caps. Equations 38, 39, and 40 are used to calculate the shear stress in the booms.

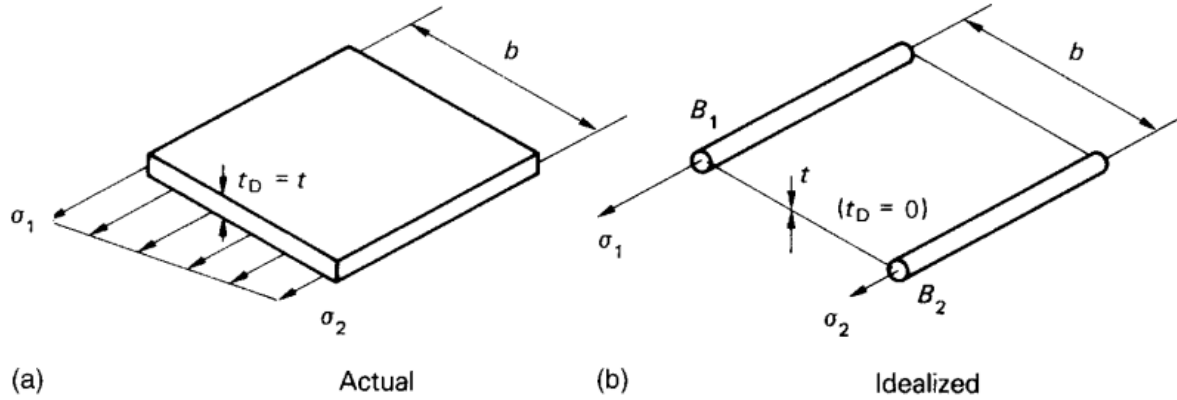


Figure 34 – Skin Panel versus Boom Panel

$$q = q_0 + q_b = q_0 + \sum_{R=1}^n \left[\frac{S_y I_{xy} - S_x I_{xx}}{I_{xx} I_{yy} - I_{xy}^2} B_r (x_r - x_c) + \frac{S_x I_{xy} - S_y I_{yy}}{I_{xx} I_{yy} - I_{xy}^2} B_r (y_r - y_c) \right] \quad (38)$$

$$B_r = A + \sum_{i=1}^n \left[\frac{t_{D(i)} b_i}{2} \right] \quad (39)$$

$$M_0 + S_y \xi_0 - S_x \eta_0 = 2Aq_0 + \sum_i^n 2q_{b,i} \Delta A_i \quad (40)$$

$$\tau = \frac{q}{t} \quad (41)$$

Where A is the area at node R, n is the number of panels that connect to node R, t_D is the panel thickness and b is the panel width. Equation 38 has two unknowns, the shear flow q and the initial shear at the cut due to torsion q_0 , which can be solved for in equation 30. The cut is an arbitrary location where the shear is first assumed to be zero as the shears are summed around the structure. The shear cut location for this analysis is the rear spar. The boom area, B_r , boom coordinates, x_r and y_r , and centroid coordinates, x_c and y_c , are known. ξ_0 and η_0 are the coordinates of the location of the cut to the origin.

The shear at all four critical locations are shown in Figures 33 thru 36

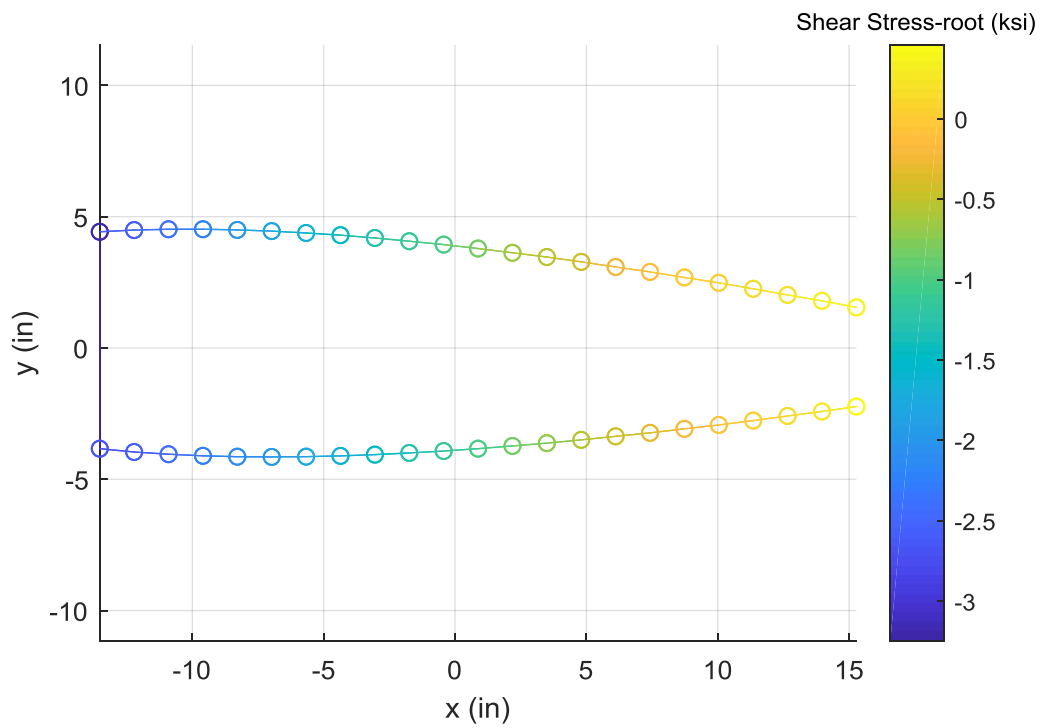


Figure 35 – LC3 45deg Flight Shear Stress at Root

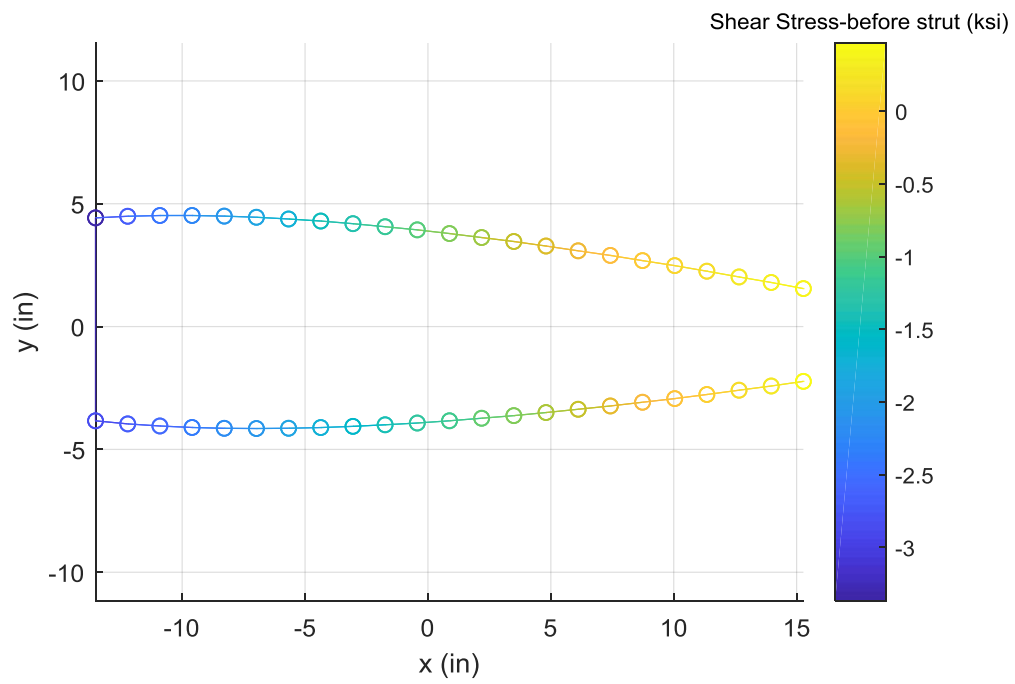


Figure 36 - LC3 45deg Flight Shear Stress before Strut

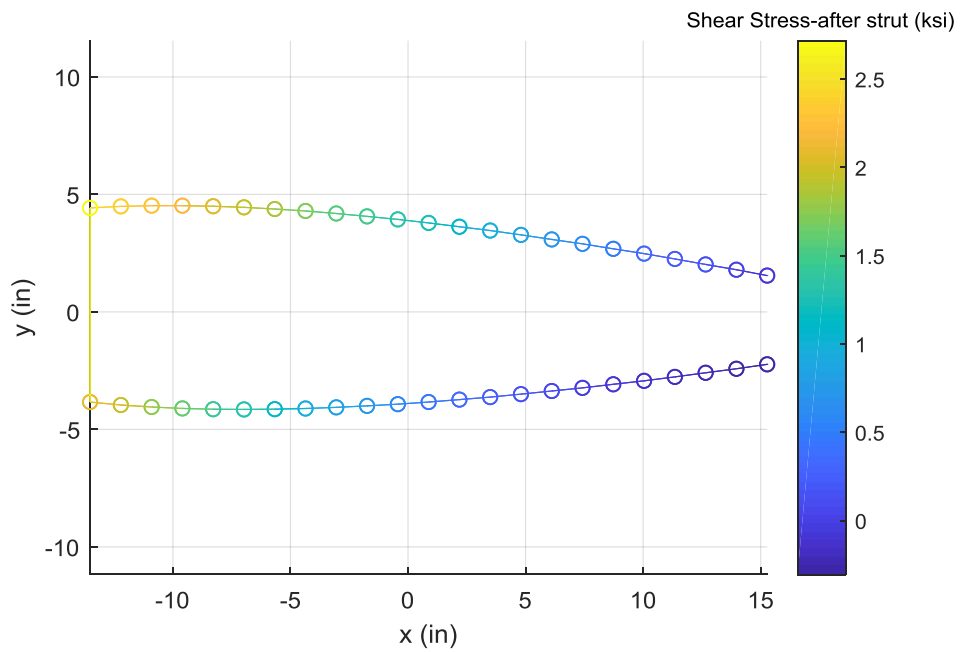


Figure 37 - LC3 45deg Flight Shear Stress after Strut

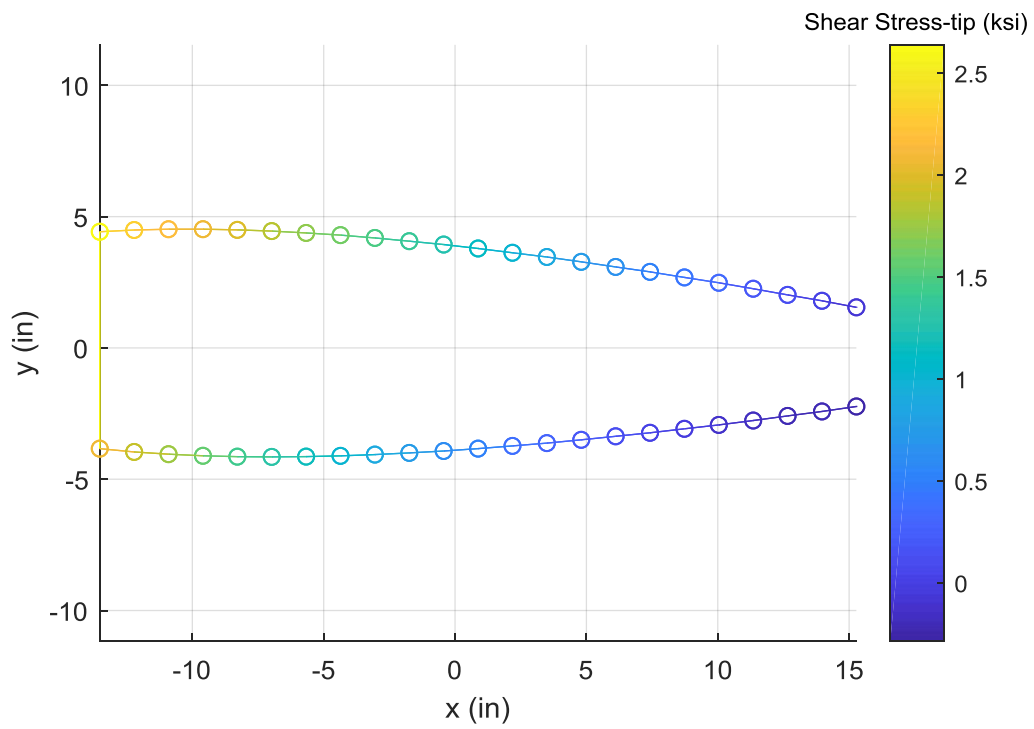


Figure 38 - LC3 45deg Flight Shear Stress at Tip

The shear stress over the entire span of the wing box can be visualized in figure 37.

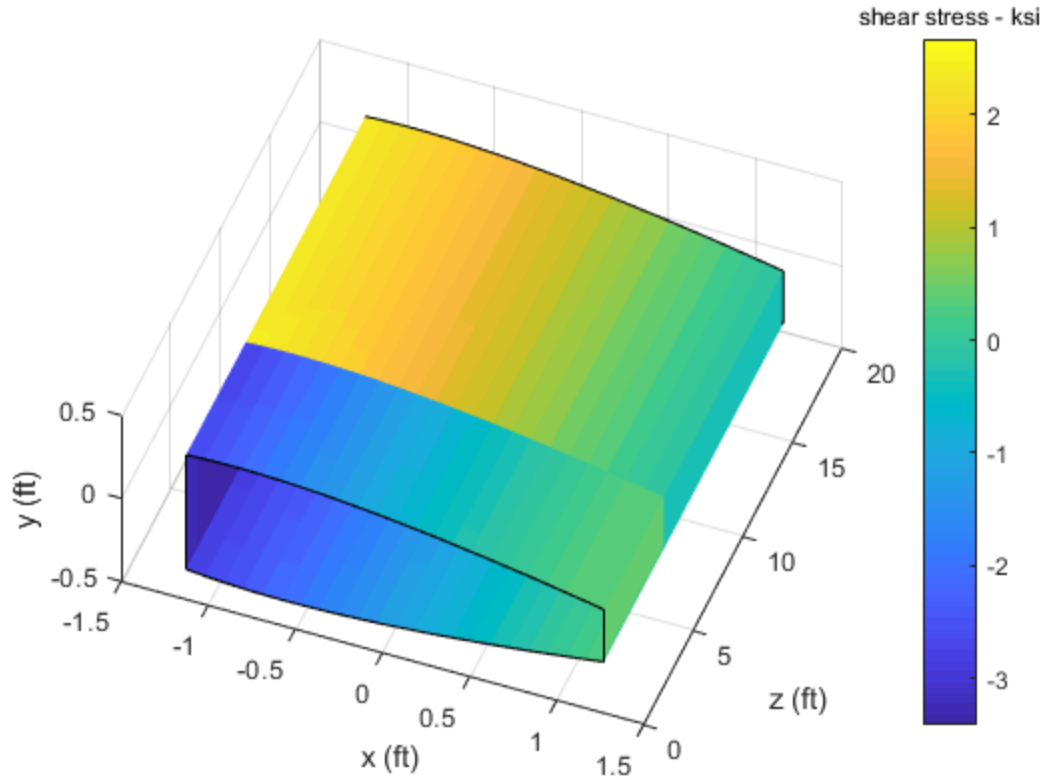


Figure 39 - LC3 45deg Flight Shear Stress over Span

The change in shear at the strut shown in figure 26 leads to the reversal of shear stress at the same location. This step change in shear stress does not consider how the strut attaches to the rib and spar structure and a more refined analysis of the connection would show a smooth transition of stress.

The normal and shear stresses can be combined into the von mises stress and checked against the yield stress to find the margin of safety for the wing, shown in equations 42 and 43. The Von Mises stress is shown in figure 39.

$$\sigma_v = \sqrt{\sigma_{zz}^2 + 3\sigma_{xy}^2} \quad (42)$$

$$MS = \frac{\sigma_y}{\sigma_v} - 1 \quad (43)$$

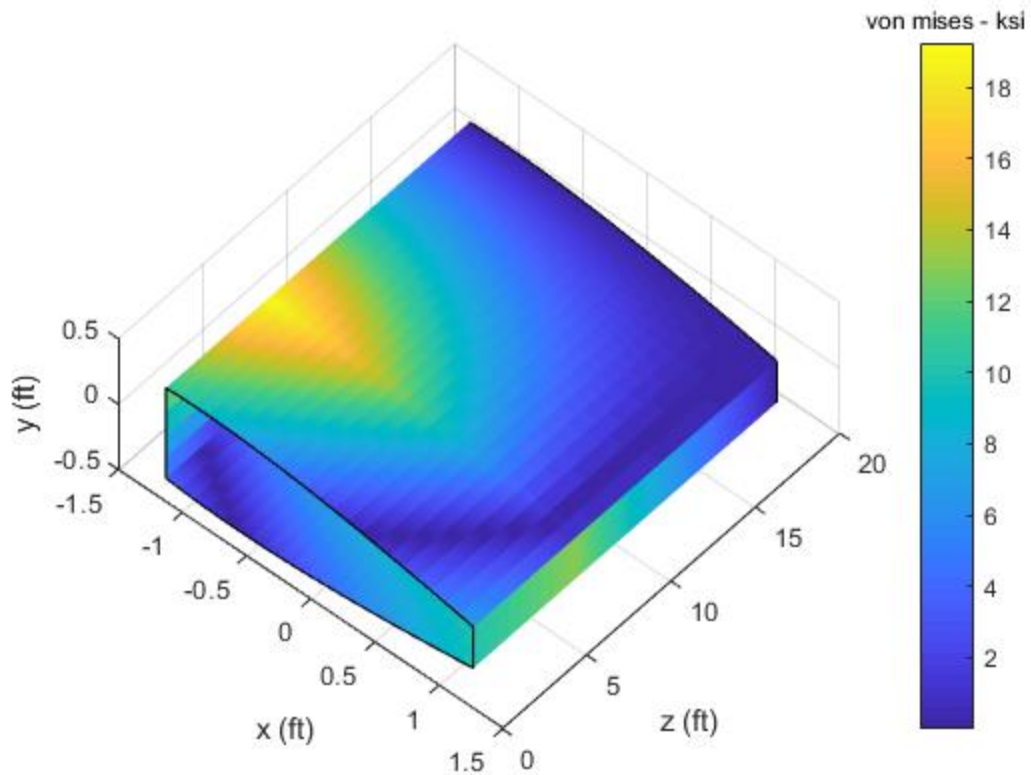


Figure 40 – Von Mises Stress LC3 45deg flight

11 Margin Summary

The margins of safety for each loadcase is summarized in Table 7.

Table 7 – Margins

Load Case		Strut x-load (lb)	Strut y-load (lb)	Skin Buckling	Stringer Yield	Fwd Spar Yield	Aft Spar Yield
LC1 Hard Landing		0	-918	3.45	12.35	12.50	13.64
LC3 Take off/Hover		0	3414	0.00	2.01	2.03	2.28
Sea level	LC3 45° flight	-377	2714	0.06	2.33	2.18	2.32
	LC4 PHAA	-712	2249	0.25	2.93	2.78	2.93
	LC5 PLAA	-296	2249	1.14	4.72	4.55	5.71
	LC6 NHAA	-328	-920	1.67	7.38	6.98	7.37
	LC7 NLAA	-161	-716	3.80	14.07	13.15	13.77
	LC8 Max Gust	-449	2249	0.68	3.85	3.67	4.26
	LC9 Min Gust	-139	-1073	3.16	11.25	10.46	11.99
8,000 ft	LC10 45° flight	-376	2714	0.07	2.19	2.19	2.35
	LC11 PHAA	-770	2249	0.11	2.49	2.39	2.48
	LC12 PLAA	-324	2249	1.11	4.72	4.53	5.60
	LC13 NHAA	-334	-920	1.63	7.24	6.85	7.24
	LC14 NLAA	-136	-716	4.31	15.64	14.64	15.38
	LC15 Max Gust	-543	2249	0.50	3.47	3.27	3.71
	LC16 Min Gust	-176	-1176	2.54	9.52	8.84	10.07

12 Finite Element Validation

A finite element model (FEM) was constructed in PATRAN and solved in NASTRAN to validate the results of this analysis. The skin and spars were modeled with shell elements and the stringers and spar caps were modeled with bars. Bush elements, rigid body elements and single point constraints were used to simulate the strut, boundary condition, and tip load application. LC2 Hover/Takeoff loads were used to compare the finite element solution to the Matlab predictions. The results are shown in table 8.

Table 8 – Matlab and FEM Comparison

LC2 Hover/Takeoff	Matlab	FEM	Percent Difference
Strut Reaction (lbs)	3414	3240	5.4%
Max Von Mises Stress (ksi)	21.2	22.6	-6.2%
Max Deflection (in)	7.1	7.3	-2.7%

The stress distribution in PATRAN for LC2 Takeoff/Hover is shown in figure 40.

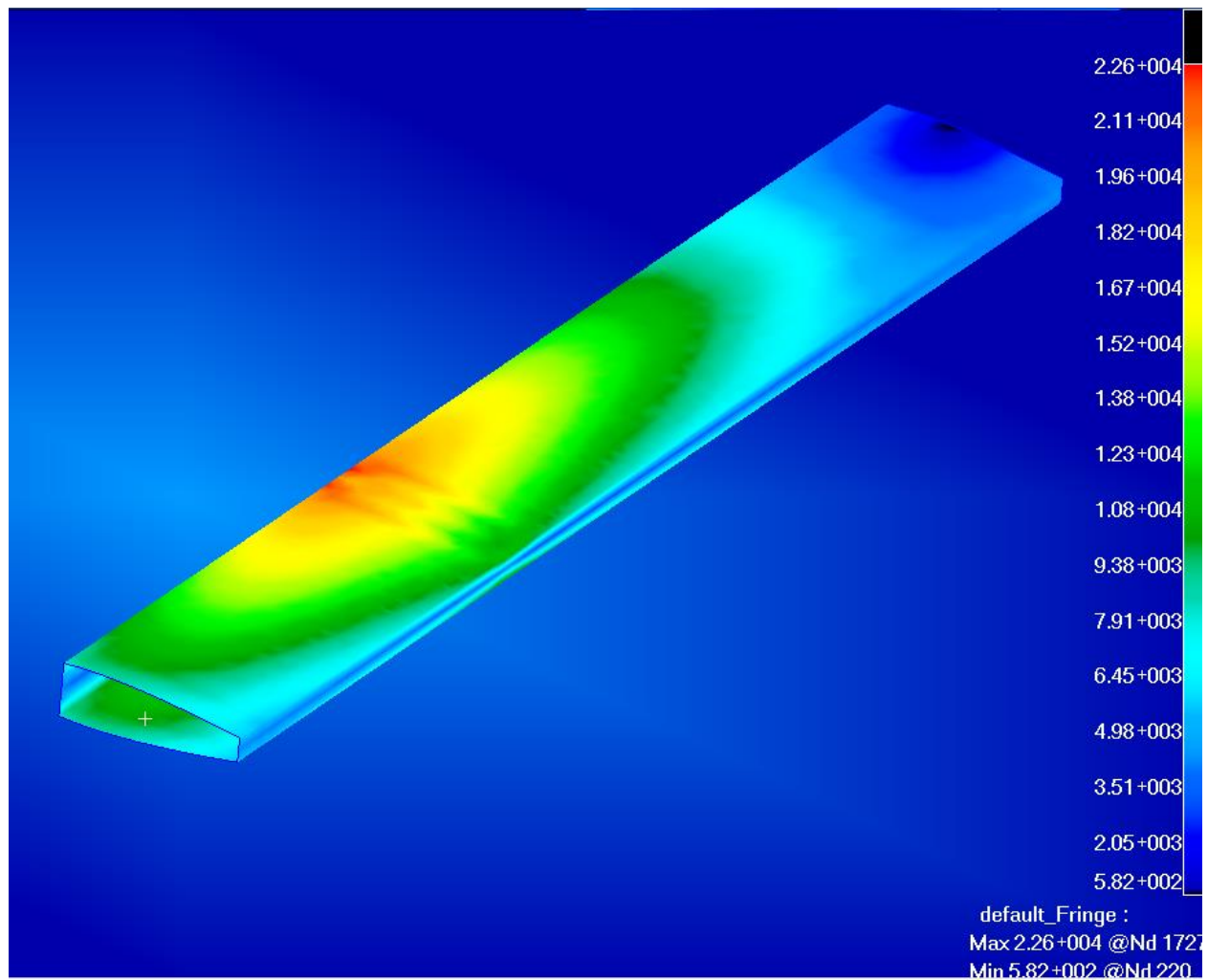


Figure 41 – LC 2 Takeoff Von Mises Stress Patran

The stress distribution from Matlab is shown in figure 41 with a uniform aspect ratio to compare to figure 40. It is shown again in figure 42 with a skewed aspect ratio to see the distribution more closely

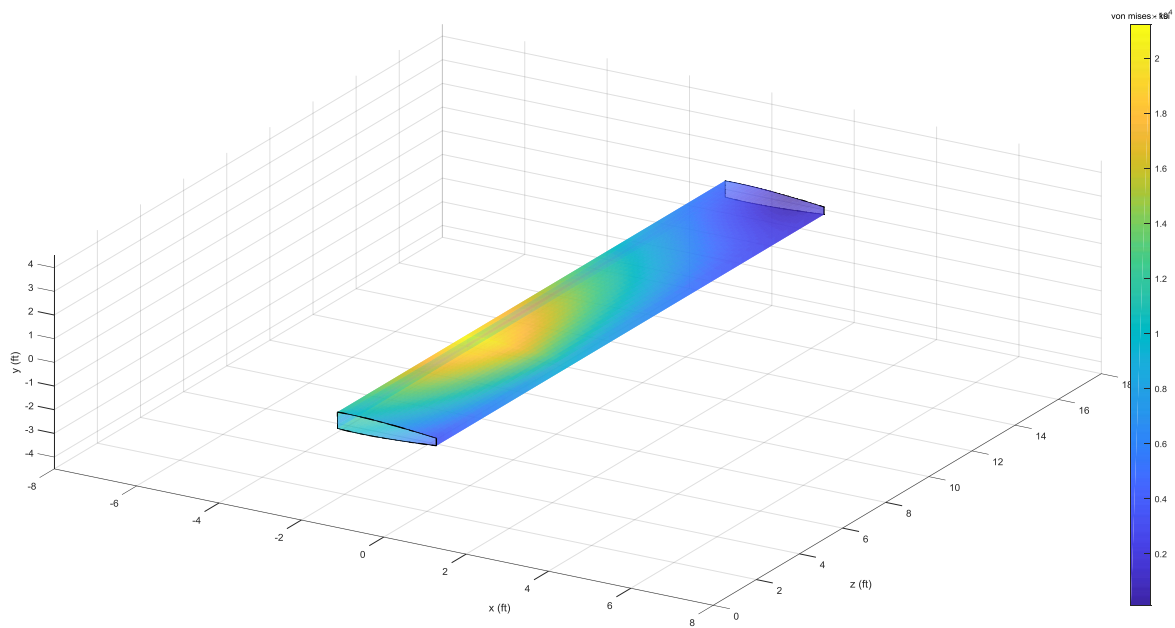


Figure 42 – LC2 Takeoff Von Mises Stress Matlab Plot with Visual Aspect Ratio 1:1:1

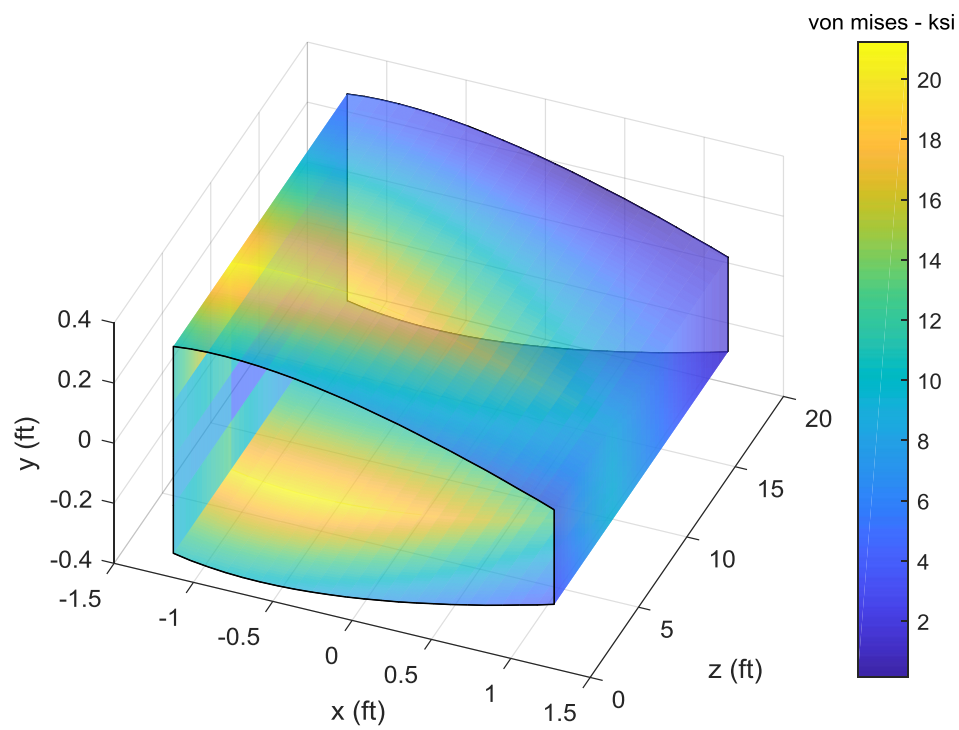


Figure 43 – LC2 Takeoff Von Mises Stress Matlab Plot

The distribution of stress between the Matlab and PATRAN results appear to be consistent lending credibility to the analysis.

13 Composite Weight Savings

There is potential improvement in the structure of the aircraft by using alternatives to metallic materials. The benefits of composites are not new to the aerospace industry but it is cost prohibitive. With a large-scale manufacturing endeavor, such as the urban air taxi, it is possible to see the benefit of both lightweight stiffness tailored material and low cost high rate production.

Aluminum is an isotropic material, meaning it has equivalent properties regardless of the orientation the material is placed in. The wing was sized to z direction normal stresses, with no normal stresses in the x and y direction. Therefore, the aluminum wing is not using all its capability in those two directions and therefor has an opportunity to increase its efficiency. The aluminum wing has an area of 4.3 square inches and a span of 36 feet. With a density of 0.1 lb/in³ density, the entire wing weighs 187 lbs.

Carbon fiber has a modulus of around 33 MSI dry and 21 MSI once it is impregnated in epoxy resin. It has almost no stiffness perpendicular to the fiber direction. (14) This property of tape plies of carbon fiber is well suited for the loading from a wing which is primarily in one direction. The yield stress of a composite laminate is extremely high well above 100 ksi. The skin thickness will be limited by the buckling strength calculated in equation 35. Although the modulus of composite is almost double that of aluminum, the thickness can only decrease by the square root of that ratio.

The increase in modulus from carbon fiber allowed the wing area to reduce to 3.3 square inches. The density of a composite laminate is only 0.06 lb/in³ so the entire wing weighs 81 lbs, less than half of its aluminum counterpart.(14) The distribution of the von mises stresses are shown in figure 43 and are not drastically different from the aluminum results.

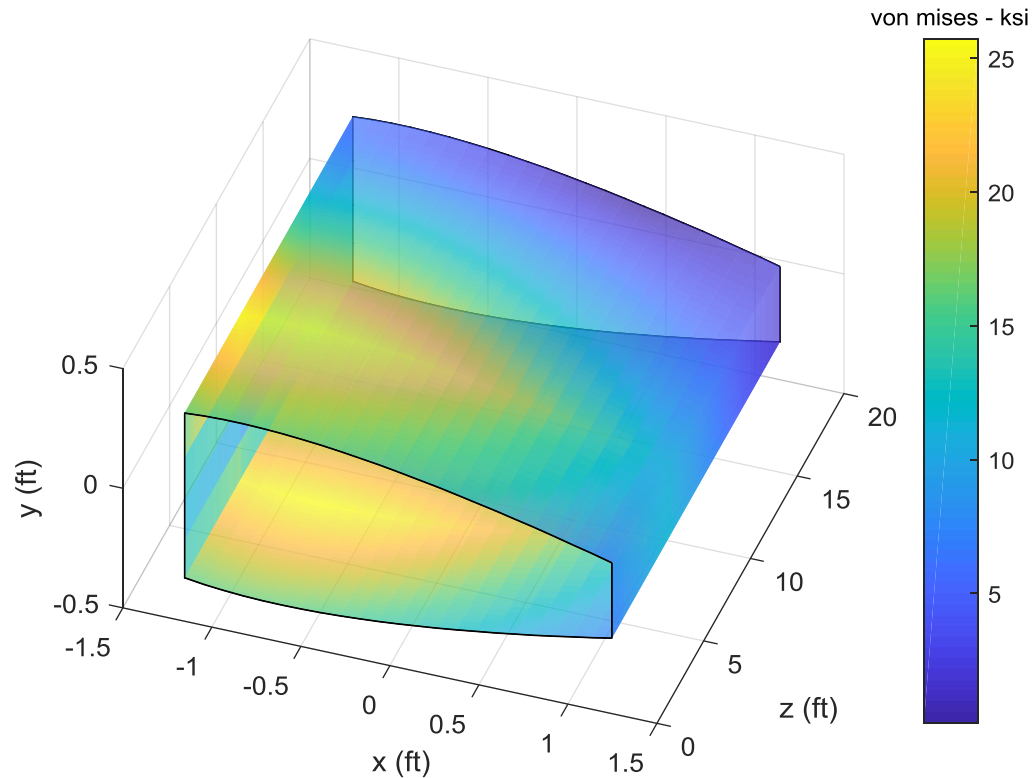


Figure 44 – LC2 Takeoff/Hover Composite Wing Box Von Mises Stress

It was decided to ignore many of the nuances of composite analysis (such as interlaminar stresses, coupling, poisons effects) for simplicity and instead use a rough methodology to find the potential of weight savings, even if it could not all be realistically achieved. There are other benefits of composites besides weight savings such as part count reduction, fastener reduction, or assembly labor savings. Even the high cost of a hand lay up for the wing could be avoided with a pull through extrusion method of manufacture.

14 Closing Statement

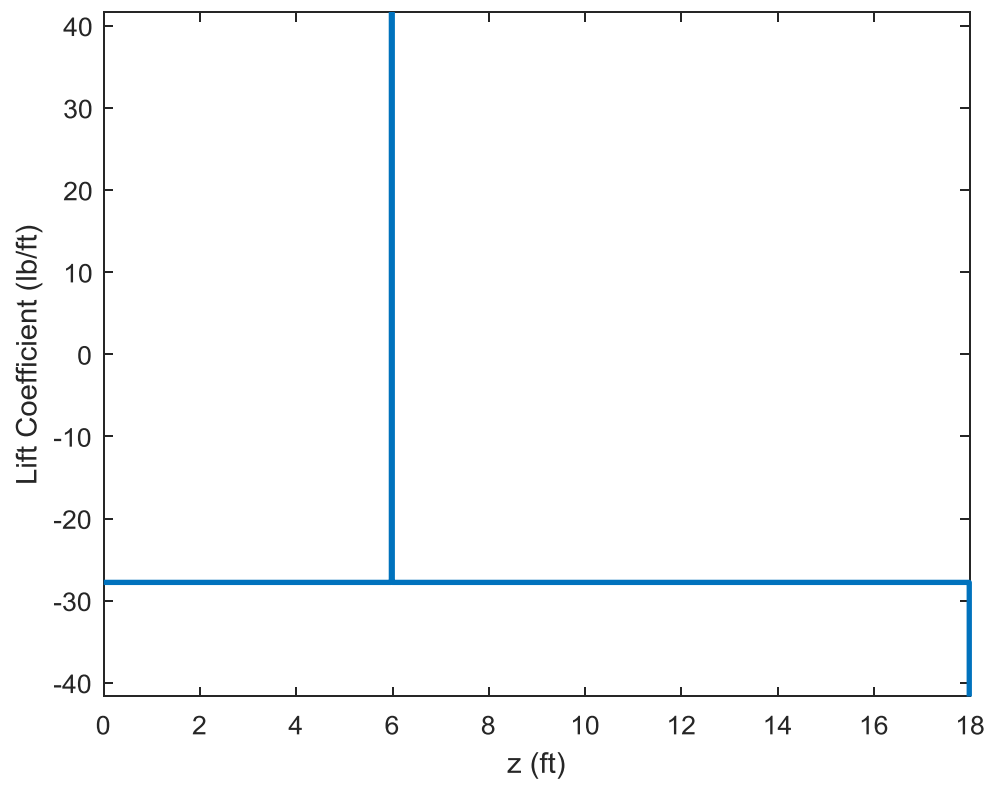
Uber published their white paper in 2016 claiming that a revolution in urban commuting was at hand. In the next five years we would have the technology for on demand aircraft optimized for short and frequent flights. The configuration (and feasibility) of this futuristic aircraft is still unclear. The goal of this paper was to design a wing that was capable of meeting Uber's requirements, and to that end it was successful.

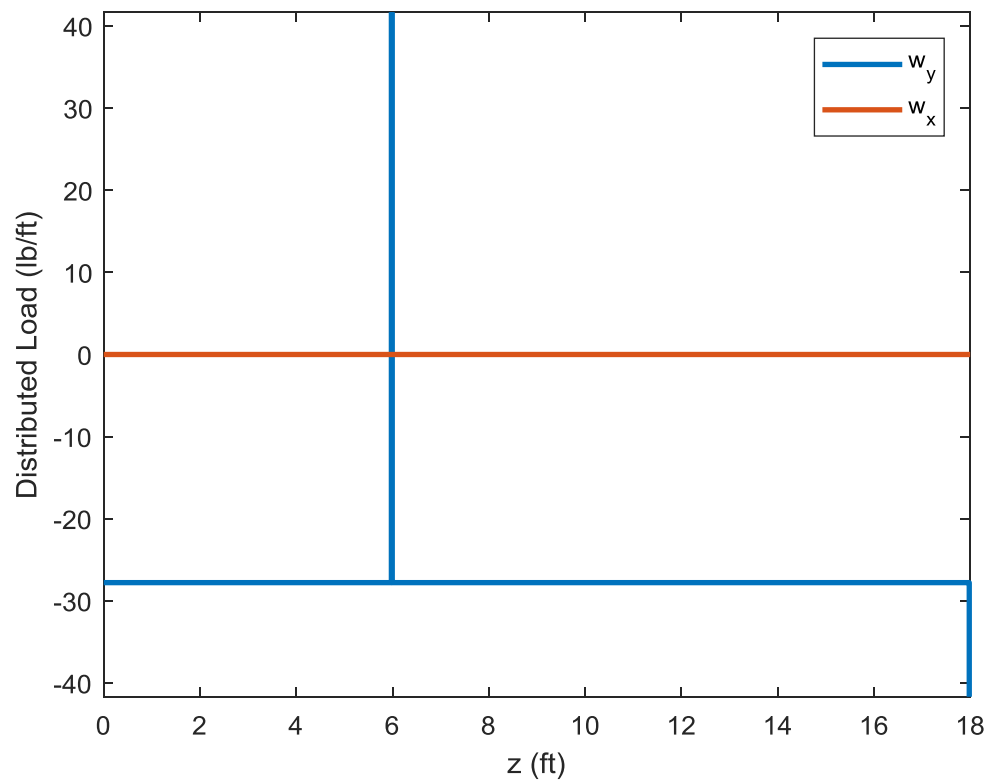
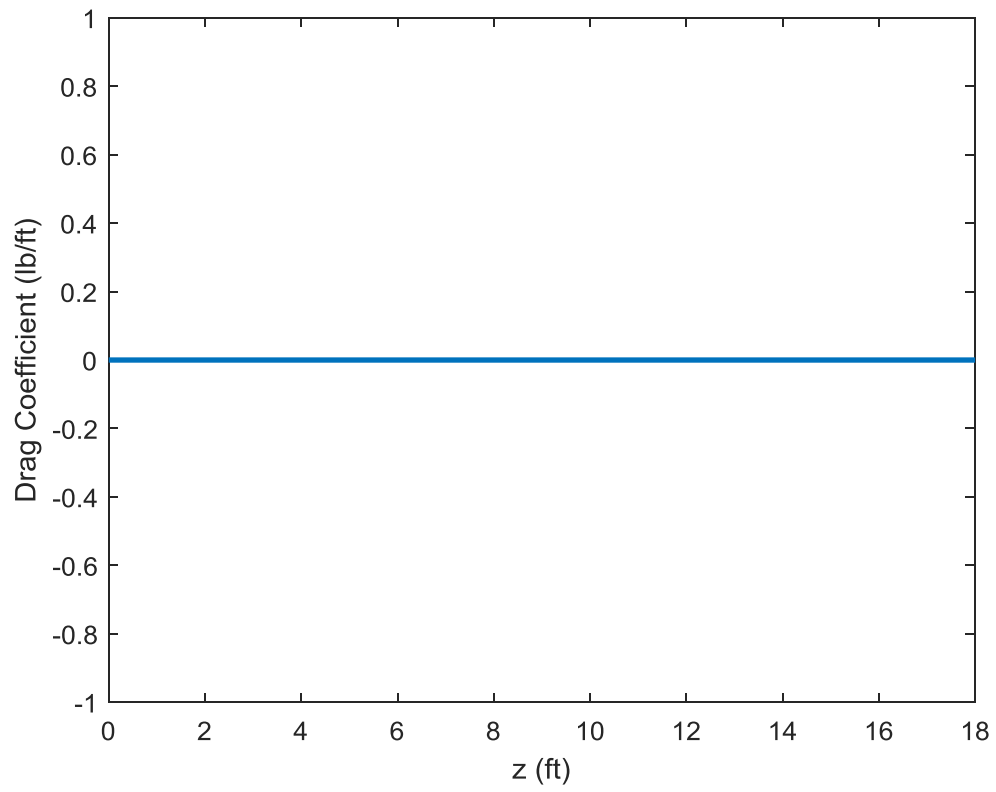
15 Works Cited

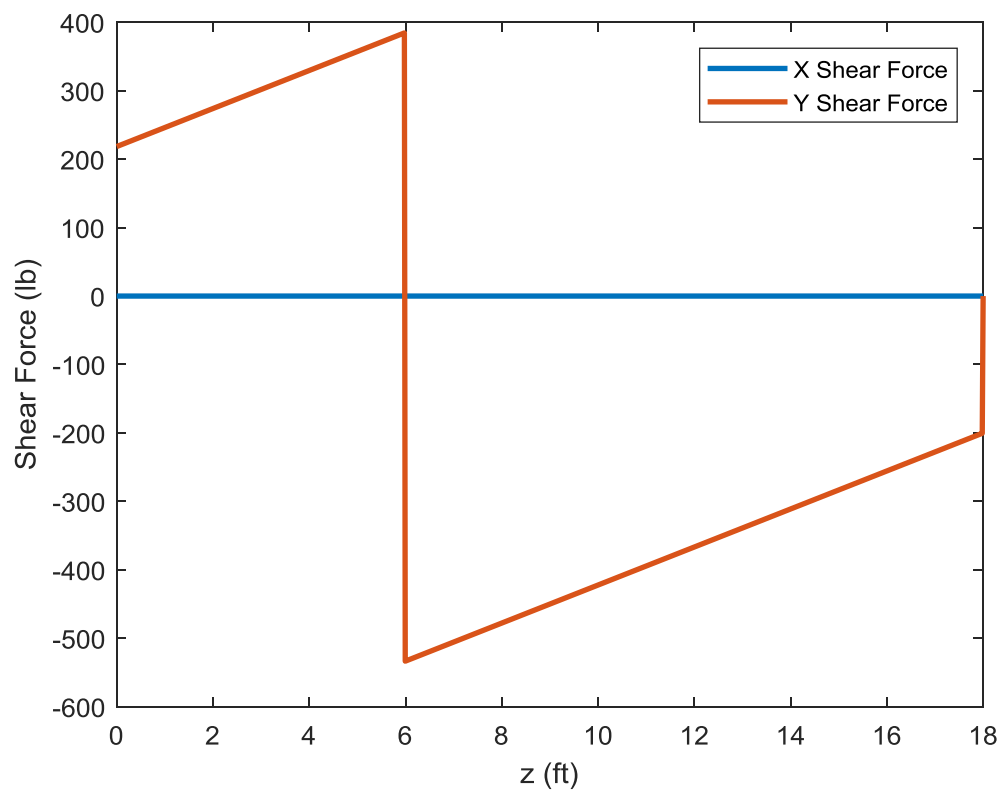
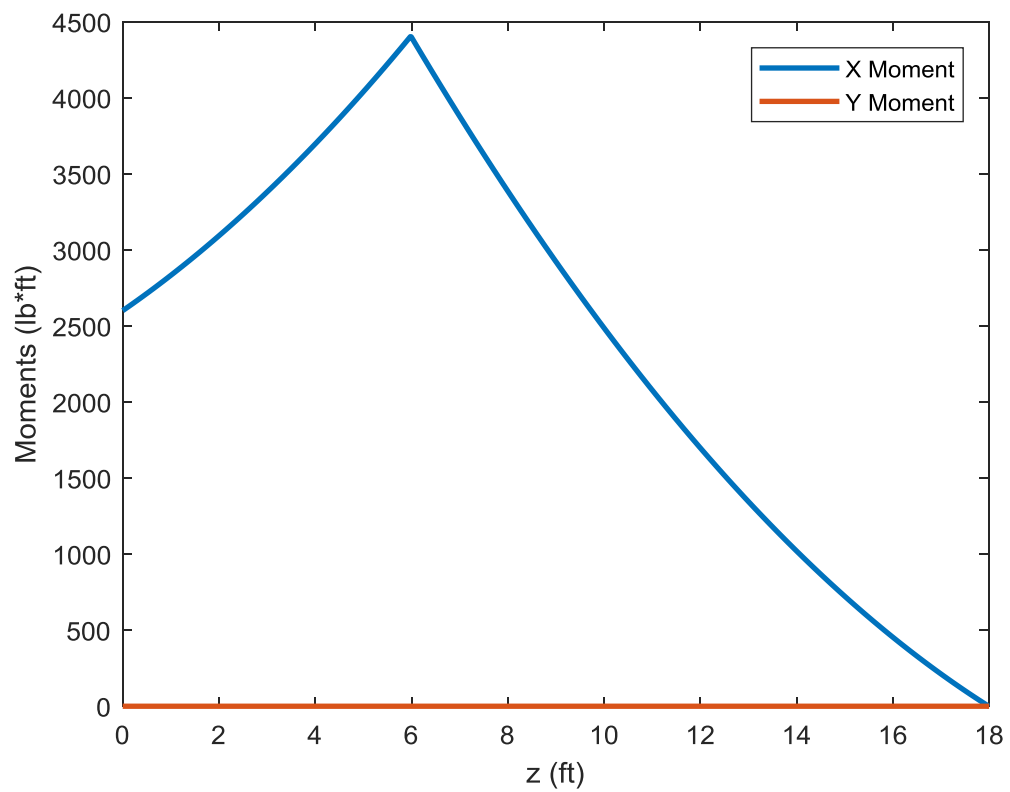
01. *Uber Elevate: Fast Forward to a Futrue of On-Demand Urban Air Transportation*. s.l. : 2016. Uber, Jeff Holden and Nikhil Goel.
02. *2016 General Aviation Statistical Databook & 2017 Industry Outlook*. s.l. : 2017. General Aviation Manufacturers Association.
03. *FAA Code of Federal Regulations Title 14 Part 23*. s.l. : 2011.
04. <https://robinsonheli.com/>.
05. <https://breakingdefense.com/2014/04/v-22-update-readiness-up-25-flight-hour-costs-down-20-since-2009/>.
06. <https://www.irs.gov/newsroom/2016-standard-mileage-rates-for-business-medical-and-moving-announced>.
07. <http://www.batteryspace.com/prod-specs/NCR18650B.pdf>.
08. [https://www.siemens.com/press/en/feature/2015/corporate/2015-03-electromotor.php?content\[\]=Corp](https://www.siemens.com/press/en/feature/2015/corporate/2015-03-electromotor.php?content[]=Corp).
09. *FAA Code of Federal Regulations Title 14 Part 27*. s.l. : 2011.
10. *MMPDS-07*. s.l. : 2012, Battelle Memorial Institute.
11. https://www.engineeringtoolbox.com/standard-atmosphere-d_604.html.
12. *Anderson, Fundamentals of Aerodynamics Sixth Edition*. New York, NY : 2017, McGraw-Hill Education.
13. *Shigley's Mechanical Engineer Design - Budynas and Nisbett*. New York, NY : 2011, McGraw Hill.
14. *Fundamentals of Composites Manufacturing, Second Edition*. s.l. : A. Brent Strong.

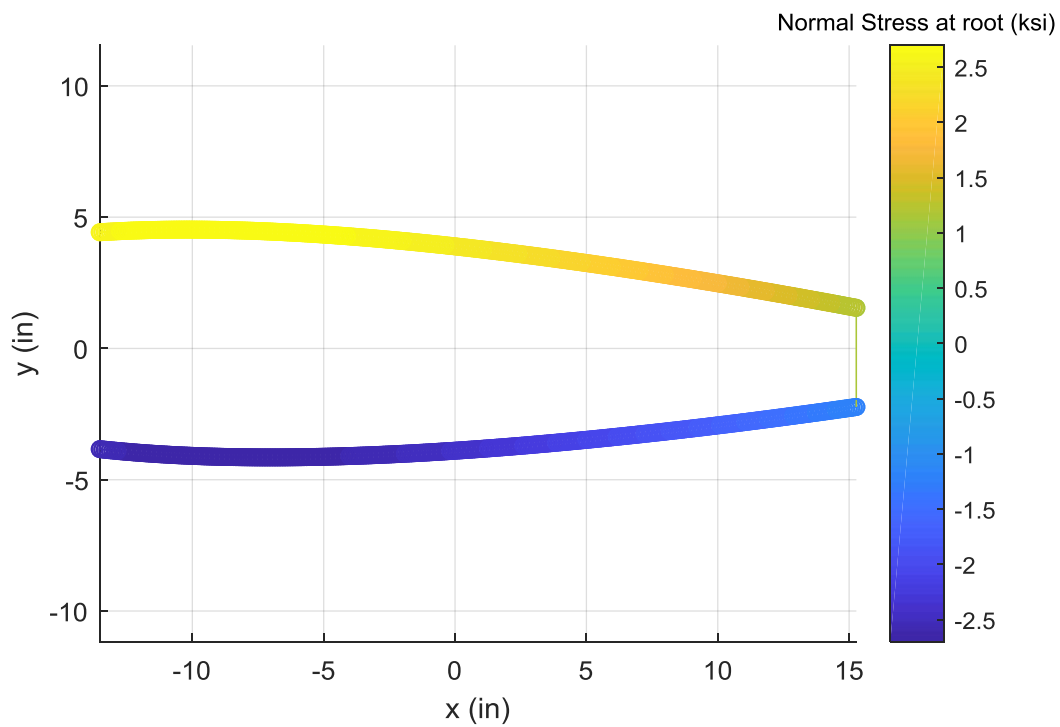
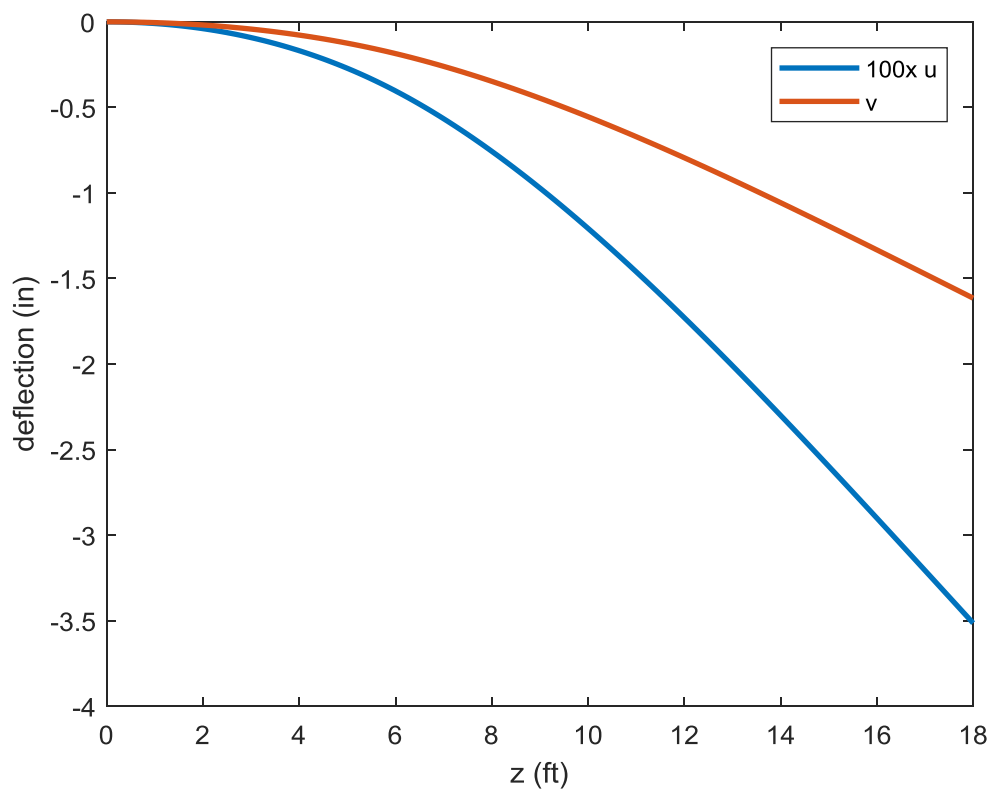
Appendix

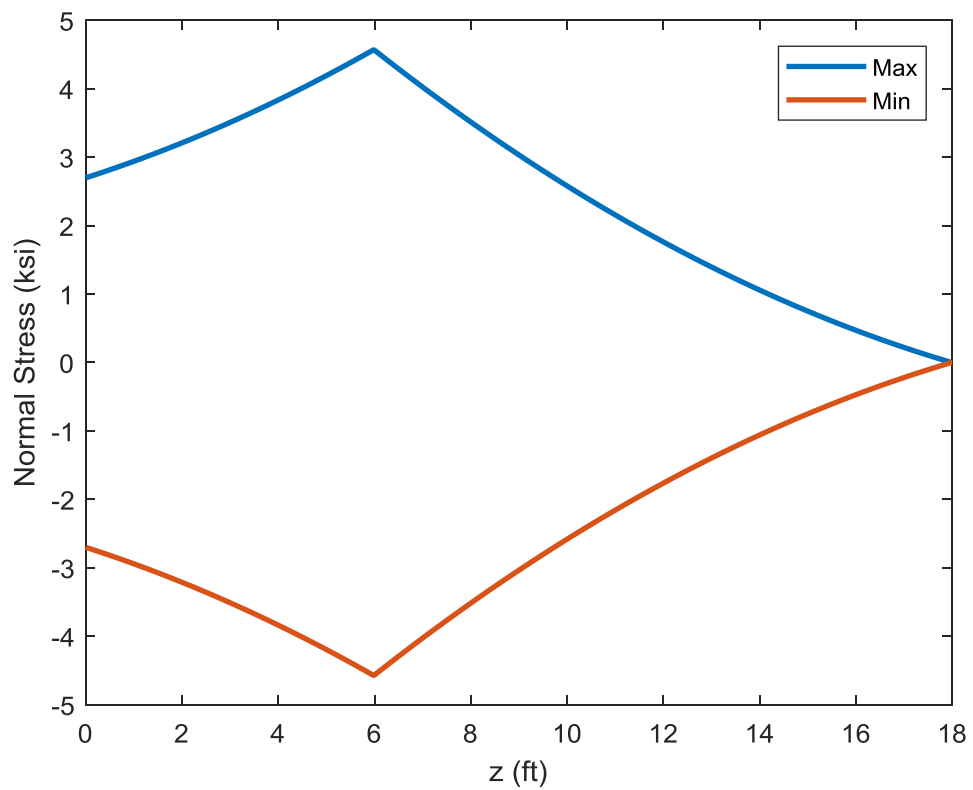
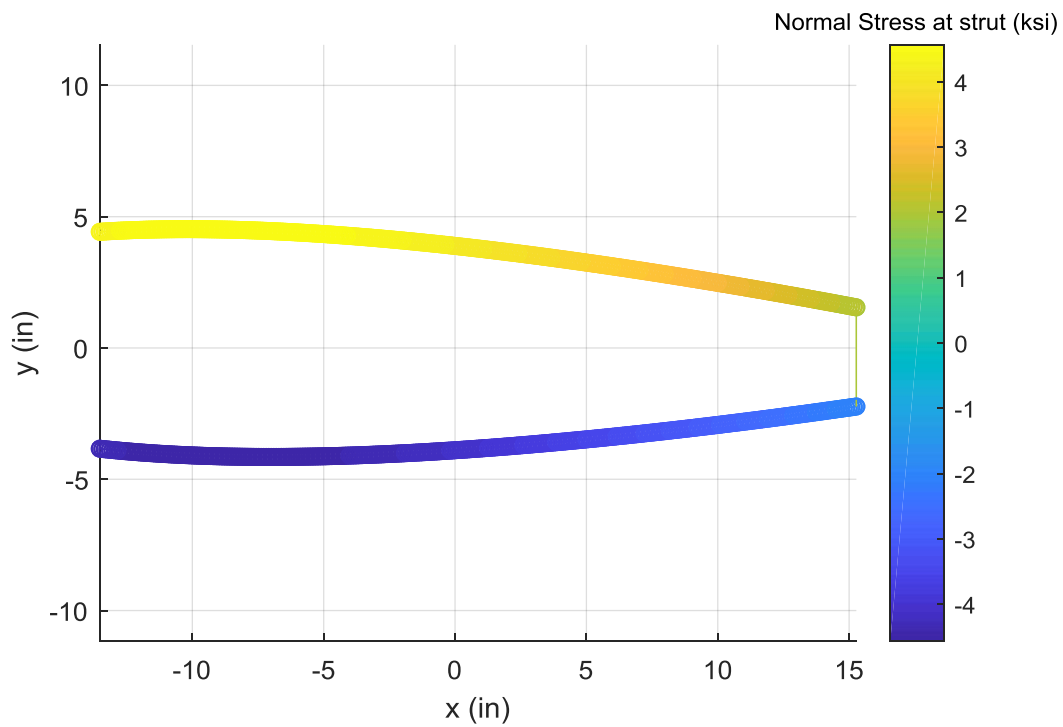
1 LC1

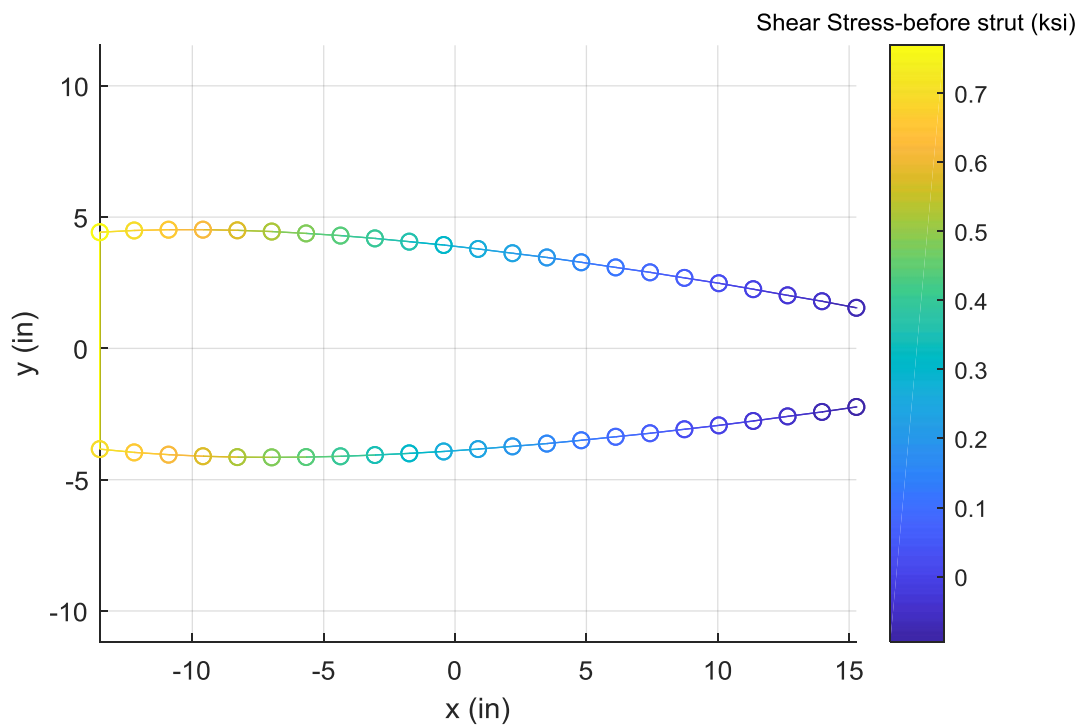
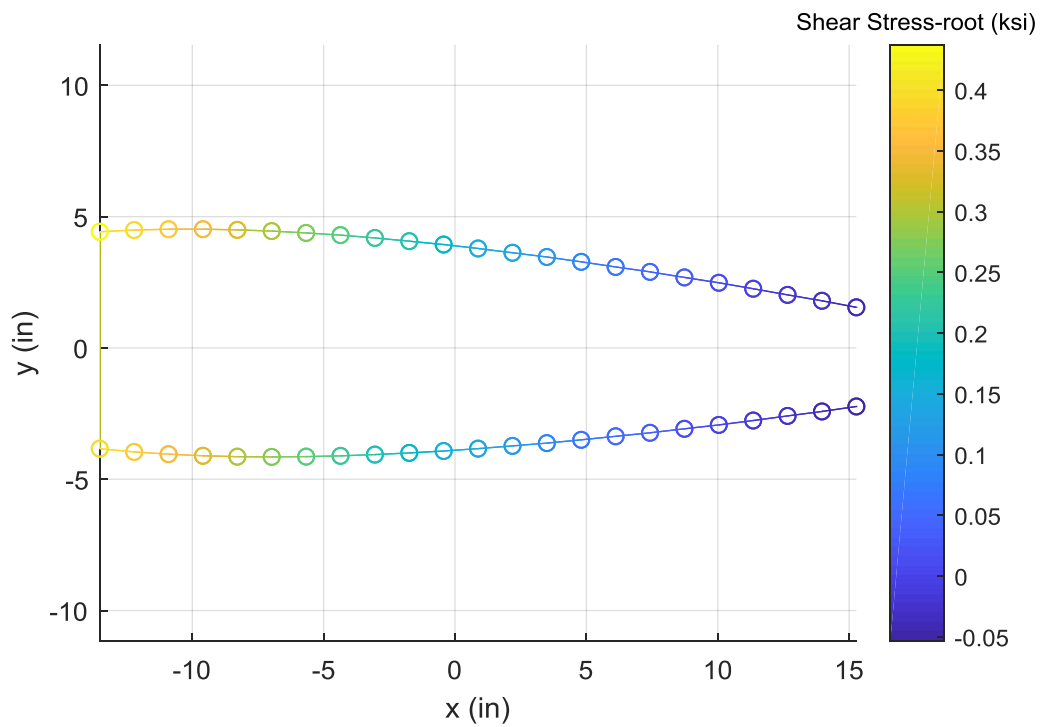


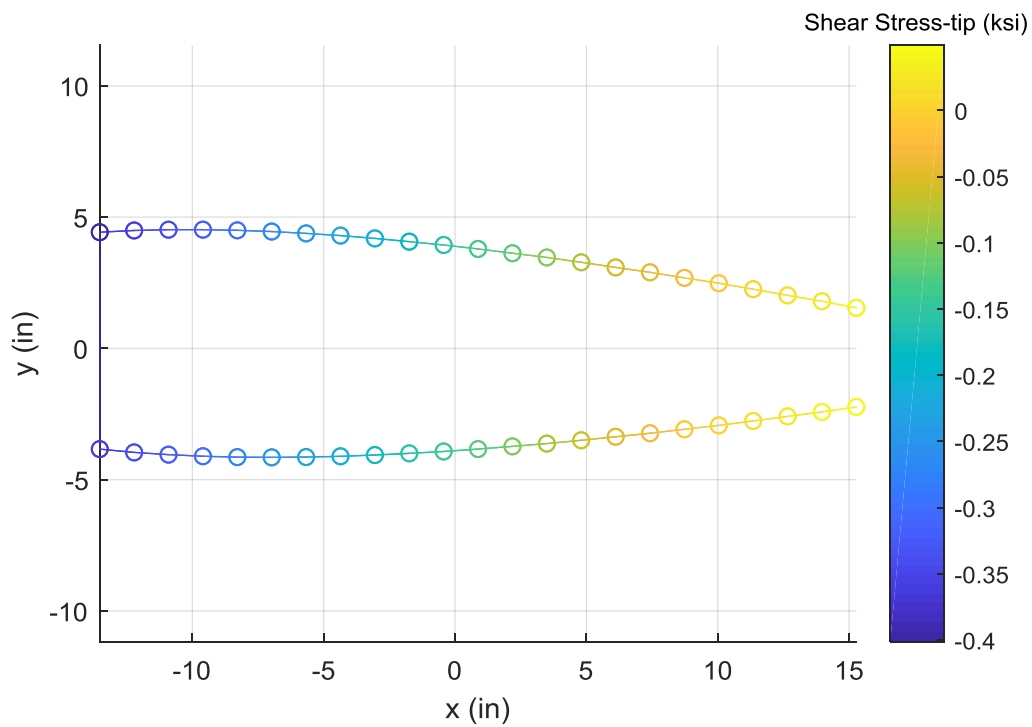
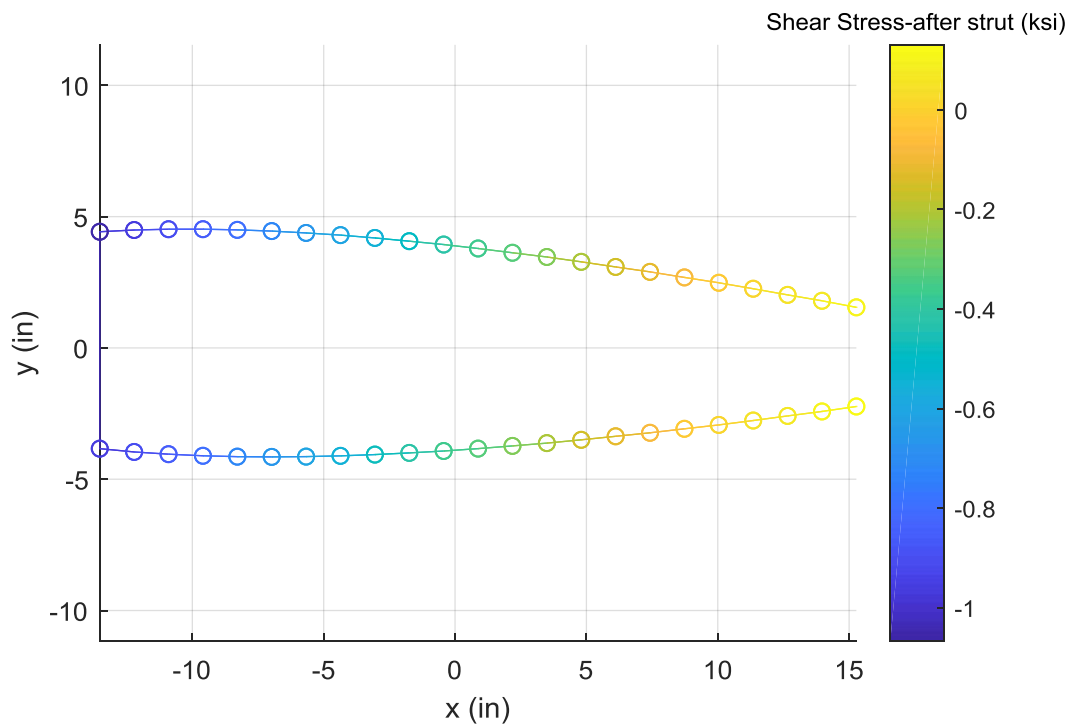


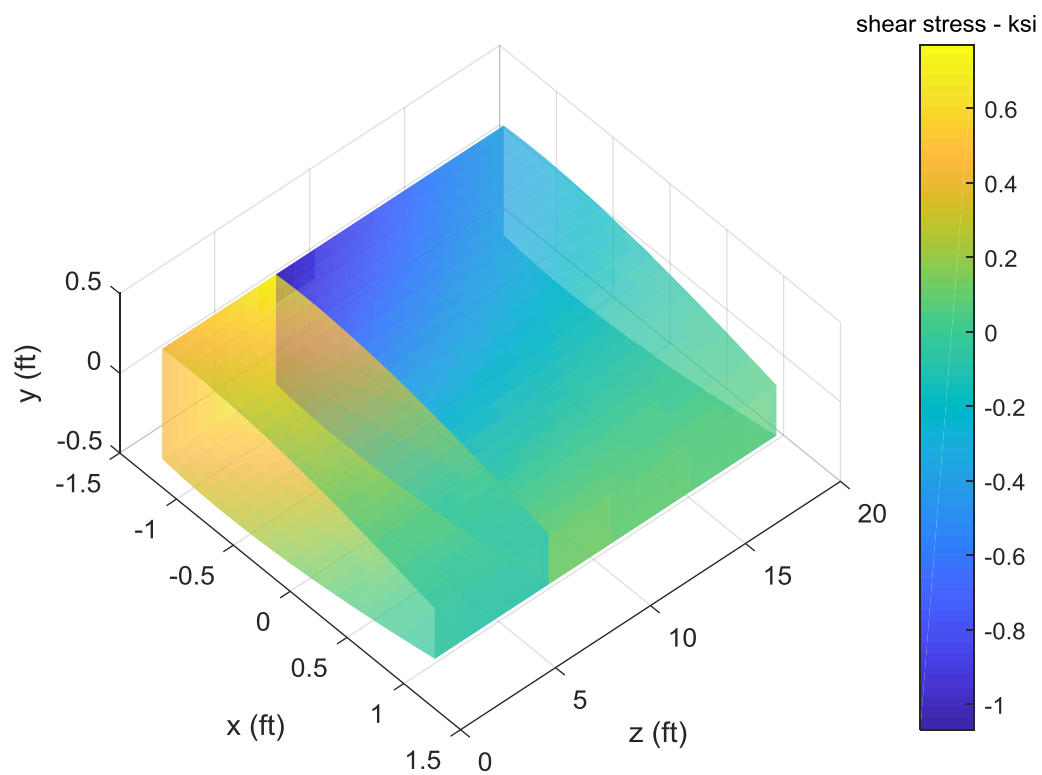
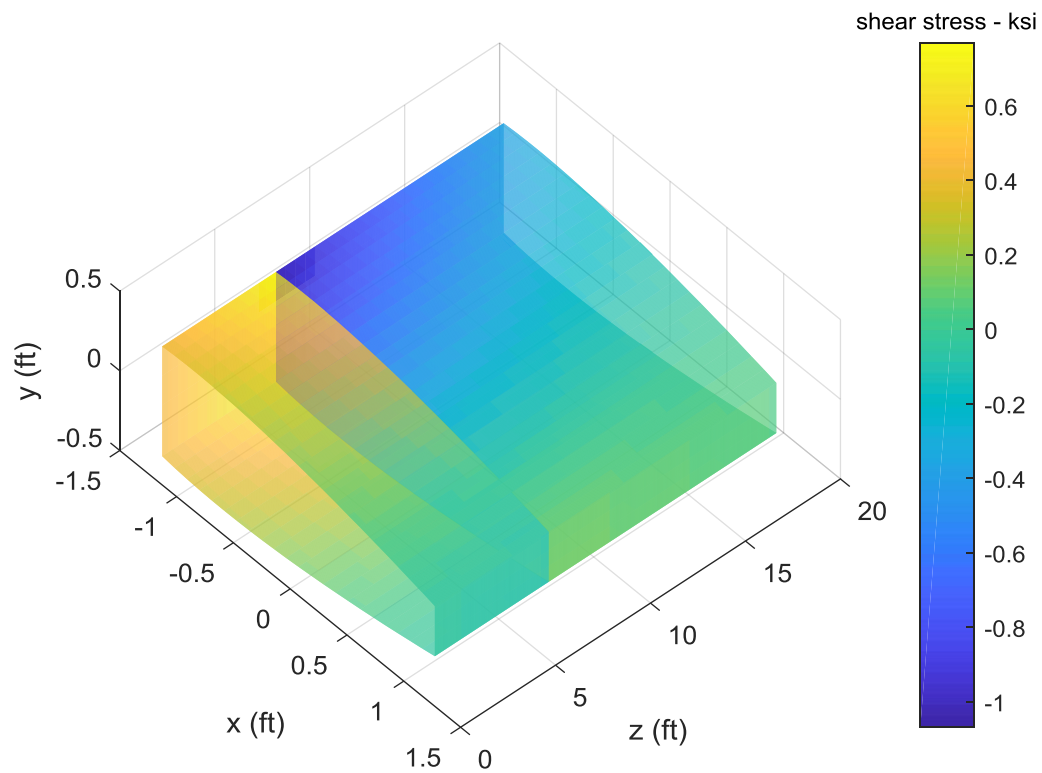












2 LC2

